

The ALMA-PILS survey: The sulphur connection between protostars and comets: IRAS 16293–2422 B and 67P/Churyumov–Gerasimenko

Maria N. Drozdovskaya^{1*}, Ewine F. van Dishoeck^{2,3}, Jes K. Jørgensen⁴, Ursina Calmonte⁵, Matthijs H. D. van der Wiel⁶, Audrey Coutens⁷, Hannah Calcutt⁴, Holger S. P. Müller⁸, Per Bjerkeli⁹, Magnus V. Persson⁹, Susanne F. Wampfler¹, Kathrin Altwegg⁵

¹ Center for Space and Habitability, Universität Bern, Sidlerstrasse 5, 3012 Bern, Switzerland

² Leiden Observatory, Leiden University, P.O. Box 9513, 2300 RA, Leiden, The Netherlands

³ Max-Planck-Institut für Extraterrestrische Physik, Giessenbachstrasse 1, 85748 Garching, Germany

⁴ Centre for Star and Planet Formation, Niels Bohr Institute & Natural History Museum of Denmark, University of Copenhagen, Øster Voldgade 5–7, 1350 Copenhagen K., Denmark

⁵ Physikalisches Institut, Universität Bern, Sidlerstrasse 5, 3012 Bern, Switzerland

⁶ ASTRON, The Netherlands Institute for Radio Astronomy, Postbus 2, 7990 AA Dwingeloo, The Netherlands

⁷ Laboratoire d'Astrophysique de Bordeaux, Univ. Bordeaux, CNRS, B18N, allée Geoffroy Saint-Hilaire, 33615 Pessac, France

⁸ I. Physikalisches Institut, Universität zu Köln, Zùlpicher Strasse 77, 50937 Köln, Germany

⁹ Department of Space, Earth and Environment, Chalmers University of Technology, Onsala Space Observatory, 439 92 Onsala, Sweden

Accepted xxx. Received xxx; in original form xxx

ABSTRACT

The evolutionary past of our Solar System can be pieced together by comparing analogous low-mass protostars with remnants of our Protosolar Nebula – comets. Sulphur-bearing molecules may be unique tracers of the joint evolution of the volatile and refractory components. ALMA Band 7 data from the large unbiased Protostellar Interferometric Line Survey (PILS) are used to search for S-bearing molecules in the outer disc-like structure, ~ 60 au from IRAS 16293–2422 B, and are compared with data on 67P/C–G stemming from the ROSINA instrument aboard *Rosetta*. Species such as SO₂, SO, OCS, CS, H₂CS, H₂S and CH₃SH are detected via at least one of their isotopologues towards IRAS 16293–2422 B. The search reveals a first-time detection of OC³³S towards this source and a tentative first-time detection of C³⁶S towards a low-mass protostar. The data show that IRAS 16293–2422 B contains much more OCS than H₂S in comparison to 67P/C–G; meanwhile, the SO/SO₂ ratio is in close agreement between the two targets. IRAS 16293–2422 B has a CH₃SH/H₂CS ratio in range of that of our Solar System (differences by a factor of 0.7 – 5.3). It is suggested that the levels of UV radiation during the initial collapse of the systems may have varied and have potentially been higher for IRAS 16293–2422 B due to its binary nature; thereby, converting more H₂S into OCS. It remains to be conclusively tested if this also promotes the formation of S-bearing complex organics. Elevated UV levels of IRAS 16293–2422 B and a warmer birth cloud of our Solar System may jointly explain the variations between the two low-mass systems.

Key words: astrochemistry – stars: protostars – comets: general – ISM: molecules.

* E-mail: maria.drozdovskaya@csh.unibe.ch

1 INTRODUCTION

Sulphur-bearing molecules have been detected in many interstellar environments from diffuse clouds to star-forming regions and rocky bodies in our Solar System. It is likely that the sulphur detected in cometary studies has its roots in the earliest diffuse phases of the interstellar medium (e.g., Lucas & Liszt 2002). However, in comparison to diffuse clouds, observations show the total sulphur budget of dense cores to be depleted by several orders of magnitude (Ruffle et al. 1999). This puzzle remains unresolved; and the missing sulphur is yet to be conclusively identified (e.g., Anderson et al. 2013). Such depletion is unique to sulphur, making it a key element in understanding the evolution of volatile and refractory components between the diffuse and dense phases.

Some of the first detections of interstellar sulphur came in the 1970s and 1980s when molecules such as CS, OCS, H₂S, SO, H₂CS and SO₂ were observed in the gas phase towards Sgr B2 and Orion A (Penzias et al. 1971; Jefferts et al. 1971; Drdla, Knapp & van Dishoeck 1989; Minh et al. 1990; Pastor et al. 1991). These detections kicked off the study of its chemistry, which suggested that in thin clouds, sulphur is predominantly in the form of S⁺ ions (Oppenheimer & Dalgarno 1974) and likely undergoes partial incorporation into refractories. Meanwhile, in dense clouds it is mostly neutral and gets incorporated into the observed volatiles via reactions with H₃⁺ (Oppenheimer & Dalgarno 1974) and grain-surface reactions (Duley, Millar & Williams 1980). Subsequent chemical models quickly showed that the net sulphur budget as seen in volatiles is severely depleted in dense clouds (Prasad & Huntress 1982). Some of the sulphur is incorporated into carbon chains such as C_nS (with $n = 1, 2, \dots$; Wlodek, Bohme & Herbst 1988; Smith et al. 1988; Millar & Herbst 1990; Hirahara et al. 1992). However, since the ionization potential of sulphur is lower than that of carbon, S⁺ may exist in regions where most of carbon is neutral, which may lead to the formation of S₂ (suggested early on by Duley, Millar & Williams 1980). In photodissociation regions (PDRs), it appears that sulphur is found in the form of CS and HCS⁺ (Jansen, van Dishoeck & Black 1994; Goicoechea et al. 2006).

Sulphur-bearing species are also seen in solid form: OCS ice was the first to be detected (Palumbo, Tielens & Tokunaga 1995; Palumbo, Geballe & Tielens 1997; Aikawa et al. 2012) and the detection of solid SO₂ followed (Boogert et al. 1997). These ices have been seen in absorption against the bright high-mass W33A protostar and account for < 5 per cent of the elemental sulphur abundance. Other sulphur-bearing ices are yet to be detected (Boogert, Gerakines & Whittet 2015). Such simple sulphur-bearing volatiles are likely formed via a combination of gas-phase reactions and grain-surface chemistry. It remains unclear where the remaining sulphur is at cold, dark prestellar conditions. More recently, sulphur-bearing complex organics have been detected. The S-containing methanol-analog, CH₃SH, has been detected in the gas phase towards the cold core B1 (Cernicharo et al. 2012); the hot core G327.3–0.6 (Gibb et al. 2000); Orion KL (Kolesniková et al. 2014); the O-type protostar IRAS 16547–4247 (Zapata et al. 2015); Sgr B2(N2) (by Linke, Frerking & Thaddeus 1979 and in the EMOCA survey by Müller et al. 2016); and IRAS 16293–2422 (Majumdar et al. 2016). The detection of the S-containing ethanol-analog, C₂H₅SH, has been reported towards Orion KL (Kolesniková et al. 2014); while searches towards Sgr B2(N2) remain uncertain (Müller et al. 2016). Such S-bearing complex organics can only form on the surfaces of grains.

Sulphur-bearing species have also been detected in numerous places in the Solar System and several comets. A large reservoir of sulphur is found on Jupiter’s moon Io, which has an atmosphere dominated by SO₂, as a result of active volcanic eruptions (e.g., Jessup, Spencer & Yelle 2007; Moullet et al. 2008, 2013). Contrary to the interstellar medium (ISM), the majority of cometary detections of sulphur-bearing molecules belong to H₂S and S₂ (A’Hearn, Schleicher & Feldman 1983; Mumma & Charnley 2011). Towards the brightest comet – Hale–Bopp, a greater diversity has been observed, including OCS, SO₂ and H₂CS. The brighter comets C/2012 F6 (Lemmon) and C/2014 Q2 (Lovejoy) have also been shown to contain CS (Biver et al. 2016). Currently, some of the most unique in-situ data are available from the *Rosetta* mission on comet 67P/Churyumov–Gerasimenko (67P/C–G hereafter; Glassmeier et al. 2007). With the Rosetta Orbiter Spectrometer for Ion and Neutral Analysis (ROSINA; Balsiger et al. 2007) aboard the orbiter, the coma has been shown to contain H₂S, atomic S, SO₂, SO, OCS, H₂CS, CS₂ and S₂ (and tentatively CS, as the mass spectrometer cannot distinguish it from CO₂) gases (Le Roy et al. 2015). Furthermore, S₃, S₄, CH₃SH, and C₂H₆S have now been detected (Calmonte et al. 2016) and information on isotopologues is available (Calmonte et al. 2017). It seems that ~ 80 per cent of sulphur is in refractories (dust) with only ~ 20 per cent hidden in volatiles (ice; see Appendix A for the details). It is likely that surface sniffing of 67P/C–G by COSAC did not reveal any sulphur-bearing species (Goesmann et al. 2015) due to a lack of mass resolution (Altwegg et al. 2017). By piecing together the sulphur puzzle from the earliest diffuse phases to the oldest cometary probes, it may be possible to disentangle the history of volatiles and refractories simultaneously, as they are formed and assembled into larger bodies.

An important parameter for the gas-phase chemistry of sulphur-bearing molecules is the initial elemental C/O ratio at the time molecules start to form, which sets the ratio between oxygen- and carbon-containing S-bearing species (e.g., as seen in the ratio between SO and CS; Watt & Charnley 1985). Additional volatiles can be formed and/or enhanced via the passage of shocks, including HS, H₂S, S₂, SO⁺ (Mitchell 1984; Pineau des Forets, Roueff & Flower 1986; Leen & Graff 1988; Turner 1992). Species such as SO and SO₂ that are produced in the gas phase via reactions with OH upon the liberation of S via sputtering, have become traditional shock tracers. Sulphur-bearing molecules have also been used to study discs via CS (e.g., Hasegawa et al. 1984; Blake, van Dishoeck & Sargent 1992) and as tracers of the centrifugal barrier (disc-envelope interface) via SO (e.g., Sakai et al. 2014).

The possible formation routes in ices of species such as S₂ have been investigated by Grim & Greenberg (1987). In their experiments, ice mixtures containing H₂S are irradiated via ultraviolet (UV) photons and the production of sulphur chains is indirectly inferred. More recently, Chen et al. (2015) have shown that energetic processing with UV of H₂S–CO ice mixtures leads to the formation of OCS and CS₂, and of H₂S–CO₂ mixtures to OCS and SO₂. It is thought that H₂S forms via the hydrogenation of atomic S and serves as a parent species for further synthesis of sulphur-bearing ices. It is suggested that SO forms on grain surfaces via oxygen addition to HS, and SO₂ forms via oxygen addition to SO and/or via the association of two SO molecules. OCS can potentially form via the addition of oxygen to CS, the addition of sulphur to CO and/or the association of HS and CO. Experiments also predict that H₂S₂ should be made on the grains via the association of two HS molecules; however, recent observational up-

per limits place it at least an order of magnitude lower in abundance than the laboratory works suggest (towards IRAS 16293–2422; Martín-Doménech et al. 2016). Neither H_2S_2 nor HS_2 have been detected with ROSINA on 67P/C–G (Calmonte et al. 2016).

This work is an attempt at piecing together the sulphur trail by comparing its budget in the warm gas on Solar System-scales around a low-mass protostar to that in our own Protosolar Nebula. For this purpose, the paper will focus on the solar-analogue IRAS 16293–2422 B, as investigated by ALMA, and the best available sample of the innate Solar Nebula – 67P/C–G, as unraveled by ROSINA measurements. IRAS 16293–2422 is an embedded low-mass Class 0 protostellar binary with a separation of $5''.1$ (or $610 - 750$ au assuming a distance of $120 - 147$ pc; Loinard et al. 2008; Ortiz-León et al. 2017), a combined luminosity of $21 \pm 5 L_\odot$ and disc-like structures around both sources, A and B. A full overview of the physical and chemical properties of the source are presented in Jørgensen et al. (2016). The single dish survey with the Caltech Submillimeter Observatory (CSO) and the James Clerk Maxwell Telescope (JCMT) detected sulphur-bearing warm ($T_{\text{kin}} \gtrsim 80$ K) dense ($\sim 10^7 \text{ cm}^{-3}$) gas tracers such as SO, ^{34}SO , S^{18}O , SO_2 , OCS, OC^{34}S , O^{13}CS , ^{18}OCS , o- and p- H_2CS , $\text{H}_2\text{C}^{34}\text{S}$, H_2^{13}CS , SiS, ^{29}SiS ; and colder ($T_{\text{kin}} \sim 40$ K) envelope species ($10^6 \sim 10^7 \text{ cm}^{-3}$) such as CS, C^{34}S , HCS^+ , HDS (Blake et al. 1994; van Dishoeck et al. 1995 and re-analysed by Schöier et al. 2002). The single dish TIMASSS survey with IRAM-30 m and JCMT-15 m facilities expanded the list with $^{34}\text{SO}_2$, ^{13}CS , C^{33}S , HDCS and C_2S (Caux et al. 2011); and CH_3SH (Majumdar et al. 2016). Interferometric observations with the Submillimeter Array (SMA) revealed the spatial distribution of CS, C^{34}S , ^{13}CS , H_2S , H_2CS , $\text{H}_2\text{C}^{34}\text{S}$, HCS^+ , OCS, O^{13}CS , SO, ^{33}SO , ^{34}SO , SO_2 , $^{33}\text{SO}_2$, $^{34}\text{SO}_2$, SO^{18}O and SO^{17}O around the binary system on scales of $\sim 190 - 380$ au, shedding light on the fact that source A is significantly richer in sulphur-bearing species than B (Jørgensen et al. 2011). IRAS 16293–2422 B has been targeted with ALMA in Band 9: lines of $^{34}\text{SO}_2$, $^{33}\text{SO}_2$ and SO were detected in emission from a warm region near source B; and a line of H_2S was found in absorption originating from the cold foreground gas (Baryshev et al. 2015). Based on ALMA Band 6 data at $\sim 0''.6 \times 0''.5$ spatial resolution, Oya et al. (2016) revealed that it is possible to derive the kinematic envelope structure around source A via OCS emission, meanwhile H_2CS traces both the envelope and the disc-like structure.

This paper presents the full inventory of sulphur-bearing molecules towards IRAS 16293–2422 B, based on ALMA Band 7 data (Jørgensen et al. 2016). Such interferometric observations make it possible to get away from the large scale outflow- and circumbinary envelope-dominated emission and to spatially resolve the thermally desorbed molecules close to the central source. The choice to focus on source B has been made, because its lines are much narrower than those observed towards source A, hence there is less line blending. This makes it ideal for studies of isotopologues and minor species. Subsequently, ratios between various molecules are compared to those deduced for the coma gases of 67P/C–G, as measured with the ROSINA instrument (Calmonte et al. 2016). Both sets of data are some of the best available for an extrasolar analogue of our Solar System and an innate Solar Nebula tracer – a comet. The differences and similarities between the two have implications for the formation history of our Solar System. Observational details are presented in Section 2 and the results are found in Section 3. Molecular ratios are computed and compared to cometary values in Section 4 and the conclusions are given in Section 5.

2 IRAS 16293–2422 OBSERVATIONS

This work is based on the large unbiased Protostellar Interferometric Line Survey (PILS²; project-id: 2013.1.00278.S, PI: Jes K. Jørgensen) of IRAS 16293–2422 carried out with ALMA in the $329 - 363$ GHz frequency range (Band 7) with a spectral resolution of 0.2 km s^{-1} and a beam size of $0''.5$ (or $60 - 74$ au in diameter, assuming a distance of $120 - 147$ pc; Loinard et al. 2008; Ortiz-León et al. 2017). The data used here are continuum subtracted based on the statistical method described in Jørgensen et al. (2016). The observations are a combination of the 12- and the 7-m dish arrays, thereby ensuring that the emission on scales up to $\sim 13''$ is recovered, while also spatially resolving the target. The root-mean-square (RMS) noise of the combined dataset is $7 - 10 \text{ mJy beam}^{-1} \text{ channel}^{-1}$ (or $4 - 5 \text{ mJy beam}^{-1} \text{ km s}^{-1}$ with beam sizes in the $0''.34 - 0''.87$ range; see table 1 of Jørgensen et al. 2016). Hereafter, $\sigma = 10 \text{ mJy beam}^{-1} \text{ channel}^{-1}$ or $5 \text{ mJy beam}^{-1} \text{ km s}^{-1}$ is adopted. Here, the dataset convolved with a uniform circular restoring beam of $0''.5$ is used. All further details on the PILS survey, including calibration, are available in Jørgensen et al. (2016).

The spectral analysis presented in the subsequent section is carried out towards a single position of the dataset – one beam (~ 60 au) offset from source B in the SW direction, which has also been the focal point of Coutens et al. (2016), Lykke et al. (2017) and Ligerink et al. (2017); and lies twice as far as the position studied in Jørgensen et al. (2016) in the same direction. The position lies within the high density inner regions of the disc-like structure of source B (called “disc” for simplicity, hereafter), hence maximizing emission; while being sufficiently far from the source to avoid absorption against the strong dust continuum (Fig. 1). IRAS 16293–2422 is associated with one collimated pair of outflow lobes in the NW-SE direction and one less collimated in the E-W direction. The studied offset point lies in the most outflow-free direction of the region to avoid any additional sources of heating. The spectrum at this position is rich in numerous narrow ($\sim 1 \text{ km s}^{-1}$) lines from various species (and at abundances a factor of 2 lower than at those seen in fig. 5 of Jørgensen et al. (2016) for the half-beam offset position in the same direction at ~ 30 au from the source, corresponding to the comet-forming zone). The recent analysis of complex organic emission in this direction from species such as glycolaldehyde, ethylene glycol, ethylene oxide, acetone and propanal indicates that the temperatures at this point are > 100 K, thus it is likely that the chosen position is probing hot inner envelope or face-on disc material heated by the protostellar B source.

3 RESULTS AND ANALYSIS

The one beam offset position from source B of IRAS 16293–2422 in the PILS Band 7 dataset was searched for lines of all known sulphur-bearing species, including those detected in 67P/C–G, and several that have been hypothesized to be present. The initial line searching and local thermal equilibrium (LTE) modelling have been carried out with CASSIS³. Thereafter, synthetic spectra have been generated with custom IDL routines. LTE is a good assumption in this case, because the densities are high at the chosen position and

² <http://youngstars.nbi.dk/PILS/>

³ CASSIS has been developed by IRAP-UPS/CNRS, <http://cassis.irap.omp.eu>

Table 1. Best-fitting parameters for detected species at the one beam offset position from source B of IRAS 16293–2422^a

| Species | # of clean lines (# of lines in range) | CDMS entry | E_{up} (K) | N (cm ⁻²) | Derived N (cm ⁻²) of isotopologues |
|---------------------------------|---|------------|---------------------|--------------------------------------|---|
| SO ₂ , $v = 0$ | 13 (101) | 64502 | 43 – 276 | 1.5×10^{15} | $N(\text{SO}_2) = 8.8 \times 10^{15,\text{e}}$ |
| ³⁴ SO ₂ | 12 (107) | 66501 | 35 – 185 | 4.0×10^{14} | |
| SO, $v = 0$ | 0 (8) | 48501 | 81 – 87 | $\leq 5.0 \times 10^{14,\text{b}}$ | |
| OCS, $v = 0$ | 0 (2) | 60503 | 237 – 254 | $\geq 2.0 \times 10^{16,\text{b,c}}$ | 2.0×10^{17} |
| OCS, $v_2 = 1$ | 4 (4) | 60504 | 986 – 1003 | | |
| O ¹³ CS | 2 (2) | 61502 | 236 – 253 | 5.0×10^{15} | $N(\text{OCS}) = 3.5 \times 10^{17,\text{d}}$ |
| OC ³⁴ S | 3 (3) | 62505 | 231 – 265 | 1.0×10^{16} | $N(\text{OCS}) = 2.2 \times 10^{17,\text{e}}$ |
| OC ³³ S | 2 (3) | 61503 | 234 – 268 | 3.0×10^{15} | $N(\text{OCS}) = 3.8 \times 10^{17,\text{f}}$ |
| ¹⁸ OCS | 3 (3) | 62506 | 238 – 272 | 5.0×10^{14} | $N(\text{OCS}) = 2.8 \times 10^{17,\text{g}}$ |
| C ³⁴ S, $v = 0, 1$ | 1 (2) | 46501 | 65 | 2.0×10^{14} | $N(\text{CS}) = 4.4 \times 10^{15,\text{e}}$ |
| C ³³ S, $v = 0, 1$ | 0 (2) | 45502 | 65 | 8.0×10^{13} | $N(\text{CS}) = 1.0 \times 10^{16,\text{f}}$ |
| C ³⁶ S | 1 (1) | 48503 | 64 | 1.4×10^{13} | $N(\text{CS}) = 6.6 \times 10^{16,\text{h}}$ |
| H ₂ CS | 9 (22) | 46509 | 102 – 419 | 1.5×10^{15} | $N(\text{H}_2\text{CS}) = 1.5 \times 10^{15}$ |
| HD ³⁴ S | 1 (7) | 37503 | 35 | 1.0×10^{15} | |
| HDCS | 6 (23) | 47504 | 98 – 322 | 1.5×10^{14} | $N(\text{H}_2\text{S}) = 1.6 \times 10^{17\text{i}-18\text{j}}$ |
| HDS | 1 (10) | 35502 | 35 | 1.6×10^{16} | $N(\text{HDS}) = 2.2 \times 10^{16,\text{e}}$ |
| CH ₃ SH, $v = 0 - 2$ | 12+ (496) | 48510 | 127 – 437 | 5.5×10^{15} | $N(\text{H}_2\text{S}) = 2.2 \times 10^{17\text{i}-18\text{j}}$ |

^a assuming a source size of 0''.5, FWHM of 1 km s⁻¹ and $T_{\text{ex}} = 125$ K^b blended^c optically thick^d assuming ¹²C/¹³C = 69 (Wilson 1999)^e assuming ³²S/³⁴S = 22 (Wilson 1999)^f no estimate for the local ISM is available, so a solar ratio of ³²S/³³S = 125 is used (Asplund et al. 2009)^g assuming ¹⁶O/¹⁸O = 557 (Wilson 1999)^h no estimate for the local ISM is available, so a solar ratio of ³²S/³⁶S = 4747 is used (Asplund et al. 2009)ⁱ assuming D/H = 0.05, as measured with single dish observations of HDS/H₂S (table 11 of van Dishoeck et al. 1995)⁴^j assuming D/H = 0.005, as recent studies suggest that single dish observations may be overestimating deuteration as a result of underestimating optical depth

thus the molecules are expected to be thermalised. This assumption has also been quantified for the case of methanol (CH₃OH) in section 5.1 of Jørgensen et al. (2016). It was shown that for the high densities probed by this dataset ($\gtrsim 3 \times 10^{10}$ cm⁻³), the deviation of excitation temperatures under the assumption of LTE from kinetic temperatures of non-LTE calculations is expected to be lower than 15 per cent. The explored grid of column densities corresponds to an uncertainty of ~ 10 per cent. Moreover, for the molecules studied in this work, all levels are well-described by a single excitation temperature.

The detected species and the best-fitting parameters, assuming a constant $T_{\text{ex}} = 125$ K for all species, are tabulated in Table 1. This value for T_{ex} has been determined as best-fitting by eye based on a grid of synthetic spectra with 25 K steps for all these species. Hence, the uncertainty on T_{ex} is ~ 20 per cent. There is no indication among this set of molecules for a different T_{ex} . A value of 125 K has also been derived for some complex organics (e.g., acetaldehyde, ethylene oxide, dimethyl ether and ketene; Lykke et al. 2017; Jørgensen et al. 2017); while other species show significantly higher excitation temperatures of ~ 300 K (e.g., glycolaldehyde, methyl formate, formamide; Coutens et al. 2016; Jørgensen et al. 2016, 2017). These variations in excitation temperatures are likely due to different molecules tracing regions of different temperatures, which is related to the different binding energies of the species and short infall time-scales of these inner regions (Jørgensen et al. 2017). Observations at an even higher spatial resolution are necessary in order to explore this in detail. It is assumed that the source

is extended and 0''.5 in size. If, both, the beam and the source distributions are Gaussian, then the observed emission is diluted by:

$$\text{beam dilution} = \text{source size}^2 / (\text{source size}^2 + \text{beam size}^2) = 0.5. \quad (1)$$

A full width half-maximum (FWHM) of 1 km s⁻¹ is taken for all species. No evidence for any deviation from this value is seen at this offset position for the sulphur-bearing molecules in this dataset. The lines are spectrally resolved into about five bins. There is no indication of any additional kinematic signature such as outflows in the lines at the spectral resolution of these data at this position. The disc-like structure around source B is face-on, so Keplerian rotation is not seen. For source A, a rotating-infalling structure is seen (Pineda et al. 2012). For sources A and B, the assumed local standard of rest (LSR) velocities are 3.2 and 2.7 km s⁻¹, respectively (Jørgensen et al. 2011). There may be a small (0.1 – 0.2 km s⁻¹) shift in the best-fitting LSR velocities between molecules tracing somewhat warmer/cooler regions (Jørgensen et al. 2017). Subsequent subsections describe the detections on a molecule by molecule basis. Isotopic ratios for the local ISM have been taken from Wilson (1999), which are an update of Wilson & Rood (1994), where available (³²S/³⁴S = 22). Otherwise, solar ratios from Asplund et al. (2009) have been employed (³²S/³³S = 125, ³²S/³⁶S = 4747). A selection of the detected lines and fitted synthetic spectra are shown in Appendix B.

Table 2. Upper limits (1σ) on the column densities of selected species at the one beam offset position from source B of IRAS 16293–2422^a

| Species | Catalogue and entry # | # of lines in range | N (cm^{-2}) |
|--|-----------------------|---------------------|---------------------------------|
| gauche-C ₂ H ₅ SH | CDMS 62523 | 1329 | $\leq 3.0 \times 10^{15}$ |
| anti-C ₂ H ₅ SH | CDMS 62524 | 470 | $\leq 6.0 \times 10^{14}$ |
| gauche-C ₂ H ₅ ³⁴ S | CDMS 64517 | 1106 | $\leq 1.0 \times 10^{15}$ |
| S ₂ | JPL 64001 | 1 | $\lesssim 2.2 \times 10^{16,k}$ |
| S ₃ | JPL 96002 | 303 | $\leq 4.0 \times 10^{15}$ |
| S ₄ | JPL 128001 | 952 | $\leq 1.0 \times 10^{16}$ |
| HS ₂ | CDMS 65509 | 227 | $\leq 5.0 \times 10^{14}$ |
| H ₂ S ₂ | CDMS 66507 | 33 | $\leq 9.0 \times 10^{14}$ |
| S ₂ O, $\nu = 0$ | CDMS 80503 | 378 | $\leq 1.0 \times 10^{15}$ |
| cis-S ₂ O ₂ | CDMS 96501 | 567 | $\leq 1.0 \times 10^{14}$ |
| HCS | CDMS 45507 | 6 | $\leq 1.0 \times 10^{15}$ |
| HSC | CDMS 45508 | 29 | $\leq 1.0 \times 10^{14}$ |
| HCS ⁺ | CDMS 45506 | 1 | $\lesssim 2.5 \times 10^{13}$ |
| DCS ⁺ | CDMS 46505 | 1 | $\lesssim 5.0 \times 10^{12}$ |
| HC ³⁴ S ⁺ | CDMS 47502 | 1 | $\lesssim 6.0 \times 10^{12}$ |
| H ₂ C ³⁴ S | CDMS 48508 | 20 | $\leq 7.0 \times 10^{13}$ |
| D ₂ CS | CDMS 48507 | 32 | $\leq 1.0 \times 10^{14}$ |
| CCS | CDMS 56502 | 14 | $\leq 4.0 \times 10^{13}$ |
| H ₂ C ₂ S | CDMS 58501 | 63 | $\leq 5.0 \times 10^{14}$ |
| c-C ₂ H ₄ S | CDMS 60509 | 191 | $\leq 1.0 \times 10^{14}$ |
| NS, $\nu = 0$ | CDMS 46515 | 20 | $\leq 2.0 \times 10^{13}$ |
| NCS | CDMS 58504 | 12 | $\leq 4.0 \times 10^{14}$ |
| HNCS, a-type ^l | CDMS 59503 | 10 | $\leq 1.0 \times 10^{14}$ |
| HSCN | CDMS 59505 | 75 | $\leq 1.0 \times 10^{14}$ |

^k not possible to derive an accurate upper limit based on one blended line, so the value from Martín-Doménech et al. (2016) is adopted, ignoring the difference in beam sizes

^l b-type (CDMS entry 59504) has two lines in range, which cannot be detected due to very high $E_{\text{up}} \sim 1700$ K

3.1 SO₂

Sulphur dioxide (SO₂) in the $\nu = 0$ state is detected based on 13 clean, non-blended lines at a column density of $1.5 \times 10^{15} \text{ cm}^{-2}$ (Fig. B1). The $\nu_2 = 1$ state is not detected due to the covered lines having very high upper energy levels ($E_u \gtrsim 800$ K). ³⁴SO₂ is detected with 12 clean lines at a column density of $4.0 \times 10^{14} \text{ cm}^{-2}$ (Fig. B2). For a ratio of $^{32}\text{S}/^{34}\text{S} = 22$, the column density of SO₂ should be $8.8 \times 10^{15} \text{ cm}^{-2}$. This value is a factor of ~ 4 higher than the column density derived from the lines of SO₂ itself. This may indicate that SO₂ is marginally optically thick at this position; however, the synthetic fits to the data do not indicate this (a higher column density leads to an overproduction of the synthetic flux in comparison to the data). Alternatively, the sulphur isotopic ratio may differ at this position and/or for this molecule from that of the local ISM, specifically $^{32}\text{S}/^{34}\text{S} = 3.8 \pm 0.5$ instead of 22. Finally, it may also be that the emission of SO₂ stems from a non-uniform emitting area, such as optically thick clumps. Such distributed clumps would still yield a smooth (beam-diluted) emission map on large scales (such as that shown in Fig. 1). ALMA Band 9 emission maps of ³⁴SO₂ at 0''.2 resolution do indeed suggest that the emission is not homogeneously distributed within the 0''.5 PILS Band 7 beam (fig. 13 of Baryshev et al. 2015). None of these possibilities can be firmly ruled out. The one beam offset position has also been searched for ³³SO₂, S¹⁸OO and S¹⁷OO; however, all these lines are very weak, with predicted emission at the noise level of the dataset.

3.2 SO

Sulphur monoxide (SO) in the $\nu = 0$ state has 8 lines in range. Only 3 are strong enough to be detected (the other 5 are weaker than 1σ) and are blended with emission from cyclopropenylidene (c-C₃H₂), methanol, ethanol (C₂H₅OH), vinyl cyanide (C₂H₃CN), glycolaldehyde (HOCH₂CHO), methyl formate (HCOOCH₃) and acetaldehyde (CH₃CHO). Therefore, the LTE fit for this molecule is less certain and only an upper limit can be derived on its column density at a value of $5.0 \times 10^{14} \text{ cm}^{-2}$ (Fig. B3). This value reflects the maximal contribution SO can have in the observed blended lines. In the $\nu = 1$ state, 7 lines are in range. However, all are predicted to be weaker than 1 mJy beam^{-1} and, thus, weaker than the noise in the dataset. The position has also been searched for ³⁴SO, ³³SO, ³⁶SO, S¹⁸O, S¹⁷O and SO⁺; however, all these lines are very weak, with predicted emission below the noise level of the dataset.

3.3 OCS

Carbonyl sulfide (OCS) in the $\nu = 0$ state has 2 lines in range that are slightly blended with lines of glycolaldehyde and ethanol, respectively (Fig. B4). The $\nu_2 = 1$ state is detected with 4 clean lines (Fig. B5). Multiple isotopologues are also detected: O¹³CS, OC³⁴S, OC³³S and ¹⁸OCS (Fig. B1–B9). This is the first time OC³³S has been detected towards this source. The presence of ³³S has been inferred previously via ³³SO₂ (Jørgensen et al. 2012) and C³³S (Caux et al. 2011). All the other isotopologues of

OCS have been detected before (Blake et al. 1994; Schöier et al. 2002; Caux et al. 2011). The dataset was also searched for ^{17}OCS , OC^{36}S , $^{18}\text{OC}^{34}\text{S}$, $^{18}\text{O}^{13}\text{CS}$, $\text{O}^{13}\text{C}^{34}\text{S}$, $\text{O}^{13}\text{C}^{33}\text{S}$; however, the predicted emission from these species is at the noise level of the dataset.

The best-fitting column density of OCS is $2.0 \times 10^{17} \text{ cm}^{-2}$, if inferred from the 4 lines of the $\nu_2 = 1$ state; and is at most $2.0 \times 10^{16} \text{ cm}^{-2}$, if approximated from the 2 blended lines of the $\nu = 0$ state. This immediately indicates that the $\nu = 0$ state is optically thick and this derived column density is a lower limit. The column density of OCS can also be inferred indirectly via its optically thin isotopologues (O^{13}CS , OC^{34}S and ^{18}OCS) and the respective local ISM isotopic ratios. The derived numbers are in Table 1 and are within a factor of two from the column density calculated from the $\nu_2 = 1$ state. They are an order of magnitude higher than that based on the $\nu = 0$ state confirming its optical thickness. The average of these four optically thin estimates is $(2.6 \pm 0.9) \times 10^{17} \text{ cm}^{-2}$. The average of the values based on just the three isotopologues is $(2.8 \pm 0.7) \times 10^{17} \text{ cm}^{-2}$ and is the best estimate of the column density of OCS at this position. As an additional check, the solar ratio of $^{32}\text{S}/^{33}\text{S} = 125$ can be used to derive the column density of OCS from its OC^{33}S isotopologue, since no estimate for the local ISM is available. This yields a value of $3.8 \times 10^{17} \text{ cm}^{-2}$, which is consistent within a factor of 1.4 with the average value derived from three other isotopologues. Alternatively, the observed column density of OC^{33}S and the estimated average column density of OCS can be used to calculate $^{32}\text{S}/^{33}\text{S}$ for IRAS 16293–2422 B to be 93 ± 11 (with 1σ significance), which is marginally sub-solar compared with the solar value of 125 at the highest end of the error bars.

3.4 CS

Carbon monosulfide (CS) in all the $\nu = 0, 1, 2, 3, 4$ vibrational states has 5 rotational lines in range. Only one of them ($\nu = 0$, $J = 7 - 6$) is expected to be strong enough to be detected ($E_u = 66 \text{ K}$ and $A_{ij} = 8.40 \times 10^{-4} \text{ s}^{-1}$), but is blended with ethyl cyanide ($\text{C}_2\text{H}_5\text{CN}$) and ethylene glycol ($(\text{CH}_2\text{OH})_2$). The C^{34}S isotopologue in the $\nu = 0, 1$ state has 2 lines in range. One is cleanly detected, while the second is predicted to be too weak for a detection due to a high value of $E_u \sim 1880 \text{ K}$. The best-fitting column density is $2.0 \times 10^{14} \text{ cm}^{-2}$ (Fig. B10). The C^{33}S isotopologue in the $\nu = 0, 1$ also has 2 lines in range. One is cleanly detected, while the second is again too weak to detect as $E_u \sim 1887 \text{ K}$. The best-fitting column density is $8.0 \times 10^{13} \text{ cm}^{-2}$ (Fig. B11). The fourth S-isotopologue C^{36}S has 1 line in range; and it is cleanly detected ($E_u = 64 \text{ K}$ and $A_{ij} = 7.66 \times 10^{-4} \text{ s}^{-1}$), giving a best-fitting column density of $1.4 \times 10^{13} \text{ cm}^{-2}$ (Fig. B12). This is a tentative first-time detection of ^{36}S towards a low-mass protostar. C^{36}S has been previously detected towards high-mass hot cores (Mauersberger et al. 1996) as a first-time detection of interstellar ^{36}S . More lines are required to confirm this detection; however, the isotopic ratios are in agreement with solar ratios. Other excitation states and isotopologues lack lines in the observed frequency range, specifically: CS in the $\nu = 1 - 0$, $2 - 1$ and $\nu = 2 - 0$ states; C^{34}S in the $\nu = 1 - 0$ state; ^{13}CS in the $\nu = 0, 1$ and $\nu = 1 - 0$ states; $^{13}\text{C}^{34}\text{S}$ and $^{13}\text{C}^{33}\text{S}$. Meanwhile, $^{13}\text{C}^{36}\text{S}$ has 1 line in range, but it is a clear non-detection. CS^+ has 2 lines in range; however, one is too weak ($A_{ij} = 7.12 \times 10^{-7} \text{ s}^{-1}$), while the other suffers from blending and absorption.

Assuming the local ISM ratio of $^{32}\text{S}/^{34}\text{S} = 22$, the column density of CS can be estimated at $4.4 \times 10^{15} \text{ cm}^{-2}$ from its

C^{34}S isotopologue. If this column density is used to fit the detected line of CS suffering from absorption, then the synthetic line width matches the observed. Thus this is the best available estimate of the column density of CS. Based on C^{33}S and C^{36}S , the column density of CS can be derived to be $1.0 \times 10^{16} \text{ cm}^{-2}$ and $6.6 \times 10^{16} \text{ cm}^{-2}$, respectively, which is factors of 2.3 and 15 larger than the value derived based on C^{34}S . This may imply that either the C^{36}S column density is poorly constrained by the single line; or that the solar isotopic ratio is not applicable for IRAS 16293–2422 B. Alternatively, the observed column densities of C^{33}S and C^{36}S in conjunction with the estimated CS column density can be used to calculate $^{32}\text{S}/^{33}\text{S}$ and $^{32}\text{S}/^{36}\text{S}$ for IRAS 16293–2422 B to be 55 ± 8 and 314 ± 44 (both with 1σ significance), i.e., a factor of 2 and an order of magnitude lower than the solar values of 125 and 4747, respectively.

3.5 H₂CS

Thioformaldehyde (H_2CS) is detected with 9 clean lines at a column density of $1.5 \times 10^{15} \text{ cm}^{-2}$ (Fig. B13). $\text{H}_2\text{C}^{34}\text{S}$ cannot be cleanly detected due to a lack of non-blended lines, thus only an upper limit of $7.0 \times 10^{13} \text{ cm}^{-2}$ can be derived (Table 2, Fig. B33). The tentative assignments of the strongest lines of $\text{H}_2\text{C}^{34}\text{S}$ at this maximal column density would imply a column density of $1.5 \times 10^{15} \text{ cm}^{-2}$ for H_2CS (assuming $^{32}\text{S}/^{34}\text{S} = 22$), thus testifying to H_2CS emission being (very close to) optically thin.

HDCS is detected with 6 clean lines at a column density of $1.5 \times 10^{14} \text{ cm}^{-2}$ (Fig. B14). Since H_2CS appears to be optically thin, the best-fitting column densities can be used to calculate the HDCS/ H_2CS ratio to be 0.1 ± 0.014 and a D/H = 0.05 ± 0.007^4 . A lower level of deuteration is ruled out based on the low quantity of $\text{H}_2\text{C}^{34}\text{S}$. This implies that thioformaldehyde is highly singly-deuterated (5 per cent), but comparable to many oxygen-bearing complex organic species (Jørgensen et al. 2017).

D_2CS is not detected with an upper limit of $1.0 \times 10^{14} \text{ cm}^{-2}$ (Table 2, Fig. B34). This yields a $\text{D}_2\text{CS}/\text{HDCS}$ ratio of < 0.67 , and a $\text{D}_2\text{CS}/\text{H}_2\text{CS}$ ratio of < 0.067 . Persson et al. (2017) derived the ratios between the deuterated isotopologues of formaldehyde (H_2CO) to be: $\text{HDCO}/\text{H}_2\text{CO} = 0.065 \pm 0.01$, $\text{D}_2\text{CO}/\text{HDCO} = 0.128_{-0.041}^{+0.033}$, and $\text{D}_2\text{CO}/\text{H}_2\text{CO} = 0.0064 \pm 0.001$. This means that in comparison to formaldehyde, the sulphur-bearing analog (thioformaldehyde) is a factor of ~ 1.5 more singly deuterated relative to its main isotopologue, at most a factor of ~ 5 more doubly-deuterated relative to its singly-deuterated isotopologue and at most a factor of ~ 10 more doubly-deuterated relative to its main isotopologue. This may suggest that thioformaldehyde forms under even more deuterium-rich conditions than formaldehyde, or that it undergoes fewer chemical reactions that would lower its level deuteration from the time of initial synthesis. Other isotopologues have not been detected: $\text{H}_2\text{C}^{33}\text{S}$ and H_2^3CS . Higher sensitivity data would be useful for ascertaining the column density of D_2CS and firmly verifying the degree of deuteration of thioformaldehyde.

3.6 H₂S

Hydrogen sulfide (H_2S) has 1 line in the observed frequency range; however, it is not detected due to a high upper energy level ($E_u = 758 \text{ K}$) and line weakness ($A_{ij} = 6.28 \times 10^{-9} \text{ s}^{-1}$). On the other

⁴ A correction for the statistical factor of 2 is applied, which assumes that deuteration events are mutually exclusive

hand, its isotopologue HDS has 10 lines in range. One of those is a clear detection at the 65σ level, while the others have upper energy levels that are too high ($E_u > 537$ K) and thus, are not expected to be strong. The best-fitting column density is $1.6 \times 10^{16} \text{ cm}^{-2}$ (Fig. B15). HD^{34}S has 7 lines in range. One is strong-enough and blend-free to be detected, while all others have upper energy levels that are too high ($E_u > 536$ K) to be stronger than the noise level. The best-fitting column density is $1.0 \times 10^{15} \text{ cm}^{-2}$ (Fig. B16). Assuming that $^{32}\text{S}/^{34}\text{S} = 22$, gives a column density of $2.2 \times 10^{16} \text{ cm}^{-2}$ for HDS, which closely (a factor of 1.4) agrees with the value derived based on its single observed line. Other isotopologues are not detected. H_2^{34}S and H_2^{33}S do not have any lines in the observed frequency range. D_2S has 4 lines in range; however, only 2 are above the noise level and both suffer from blending, thus no clear detection is possible. D_2^{34}S has 2 lines in range, but one is blended with a strong absorption feature; and the other with emission lines of acetaldehyde and the ^{13}C -isotopologue of ethyl cyanide ($\text{C}_2\text{H}_5^{13}\text{CN}$); thus, no confident detection can be claimed.

Assuming $\text{D}/\text{H} = 0.05$, as measured with single dish observations of $\text{HDS}/\text{H}_2\text{S}$ (table 11 of van Dishoeck et al. 1995⁴), the column density of H_2S can be estimated from HDS and HD^{34}S (Table 1). The average of these two values of $(1.9 \pm 0.3) \times 10^{17} \text{ cm}^{-2}$ is the best estimate of the column density of H_2S at this position. It is possible that single dish observations may be overestimating deuteration, either because of sampling colder material or as a result of underestimating optical thickness of the main species. The lowest D/H ratio seen towards IRAS 16293-2422 is 0.01 (1 per cent) for HNCO (Coutens et al. 2016). To account for this other extreme for the case of H_2S , a $\text{D}/\text{H} = 0.005$ may be assumed, increasing the best estimate to $(1.9 \pm 0.3) \times 10^{18} \text{ cm}^{-2}$.

The previously obtained SMA observations of IRAS 16293–2422 have detected a line of H_2S around ~ 216.71 GHz (see fig. 6 of Jørgensen et al. 2011). LTE modelling assuming a beam size of $3''$, a spectral resolution of 0.56 km s^{-1} (as given in table 1 of Jørgensen et al. 2011), FWHM of 1 km s^{-1} and a source size of $0''.5$ (as assumed for the ALMA observations) shows that the line is optically thick. In order to match the observed line intensity of $\sim 2 \text{ Jy beam}^{-1}$, a larger source size is necessary. Upon the assumption of a source $1''$ in size, the lower limit on the column density of H_2S is $4.0 \times 10^{16} \text{ cm}^{-2}$. This illustrates the uncertainty in the emitting area of this molecule. Alternatively, a non-detection of the sole line in range of the SMA observations of H_2^{34}S at ~ 226.70 GHz does not yield a strongly constraining column density estimate. Assuming the same parameters, in order to be weaker than the SMA 3σ noise level (where $\sigma = 0.24 \text{ Jy beam}^{-1} \text{ channel}^{-1}$; table 1 of Jørgensen et al. 2011), the column density of H_2^{34}S must not exceed $4.0 \times 10^{19} \text{ cm}^{-2}$. Assuming $^{32}\text{S}/^{34}\text{S} = 22$, the upper limit on the column density of H_2S is $8.8 \times 10^{20} \text{ cm}^{-2}$. This is consistent with the limits obtained with the uncertain limit obtained from HDS. Dedicated high resolution ALMA observations are needed in order to constrain the spatial distribution and column density of H_2S .

3.7 CH_3SH and other species

Methyl mercaptan (CH_3SH , also known as methanethiol) in the $\nu = 0 - 2$ state is detected with more than 12 clean lines at a column density of $5.5 \times 10^{15} \text{ cm}^{-2}$ (Fig. B17), which is comparable to the column density of H_2CS . Thioformaldehyde is a likely precursor for methyl mercaptan’s grain-surface formation pathways, analogously to formaldehyde being a precursor for methanol.

No other sulphur-bearing species were detected towards the one beam offset position; however, selected 1σ upper limits have

been derived and are given in Table 2 (Fig. B18- B41). The values correspond to the maximal column densities at the fixed $T_{\text{ex}} = 125$ K that the species can have in order to not exceed the observed flux at the frequencies of their emission lines. The obtained upper limits for all three versions of ethyl mercaptan ($\text{C}_2\text{H}_5\text{SH}$) are lower than the observed column density of methyl mercaptan by at most an order of magnitude, which is consistent with it being a step-up in chemical complexity.

The derived upper limits for the column densities of HS_2 and H_2S_2 are more constraining than those obtained by Martín-Doménech et al. (2016) owing to the much smaller beam size of the PILS Band 7 data. It is not possible to obtain an accurate upper limit for S_2 as only one line is covered in this dataset; however, the upper limit derived by Martín-Doménech et al. (2016) in a much larger beam size based on two lines is consistent with the observed non-detection. Carbon-sulphur chains larger than CS , e.g., C_2S , are not detected.

Upper limits on other likely carriers of sulphur in conjunction with H, C, O and N atoms are low (almost all $\lesssim 10^{15} \text{ cm}^{-2}$, compared with $\gtrsim 10^{17} \text{ cm}^{-2}$ for OCS and H_2S), which indicates that the dominating volatile sulphur reservoirs have been accounted for. The only remaining untapped sulphur reservoir would be the refractory/dust component. All other species that were not detected at this position are listed in Appendix D.

3.8 Integrated intensity maps

In order to gain insight into the spatial distribution of the emission of sulphur-bearing species, integrated intensity maps of two $^{34}\text{SO}_2$, $\nu = 0$ transitions (at 342.332 and 345.929 GHz) are displayed in Fig. 1. This molecule has been chosen as it is firmly detected with many lines; and its emission is optically thin, without a doubt, at the one beam offset position from IRAS 16293–2422 B. The pixels in the maps are $0''.1 \times 0''.1$ in order to comfortably oversample the spatial resolution of $0''.5$ of the synthesized beam. The integration is performed over 9 spectral bins (one containing the line frequency and 4 to each side of that bin). Hence, the integrated maps cover $\pm 0.9 \text{ km s}^{-1}$ around the source velocity of B of 2.7 km s^{-1} (i.e., v_{lsr} from $+1.9$ to $+3.6 \text{ km s}^{-1}$ at the spectral resolution of the data of 0.244 MHz or 0.2 km s^{-1}). This implies that the maps are appropriate for the emission stemming from quiescent gas near source B; however, near source A they are less representative even though the systemic velocity of 3.2 km s^{-1} of source A is covered. All emission lines near source A are likely wider than 2 km s^{-1} ; thus, some of the flux from the line wings is missed when integrating over just 9 bins. Moreover, there is a steep velocity gradient around source A. Integration over a wider velocity range will pollute the maps with emission from other species. In fact, even with integration over this velocity range already leads to contamination by emission from broadened neighbouring lines. Bearing in mind these limitations, Fig. 1 clearly shows that source A has stronger emission in $^{34}\text{SO}_2$ and also on larger scales. The 346 GHz line shows a higher flux than the 342 GHz line around source B, while little difference is seen around source A. Since emission in two lines from the same molecule differs spatially, the physical conditions exciting the $^{34}\text{SO}_2$ molecule must also differ around the two sources.

These maps show convincingly that the $^{34}\text{SO}_2$ emission near source B is dominated by material on small scales either from the disc or the inner envelope (barely no difference is seen when analyzing the 12-m data instead of the combination with ACA). For the 342 GHz line of $^{34}\text{SO}_2$, the line peaks at $\sim 38 \text{ mJy beam}^{-1}$

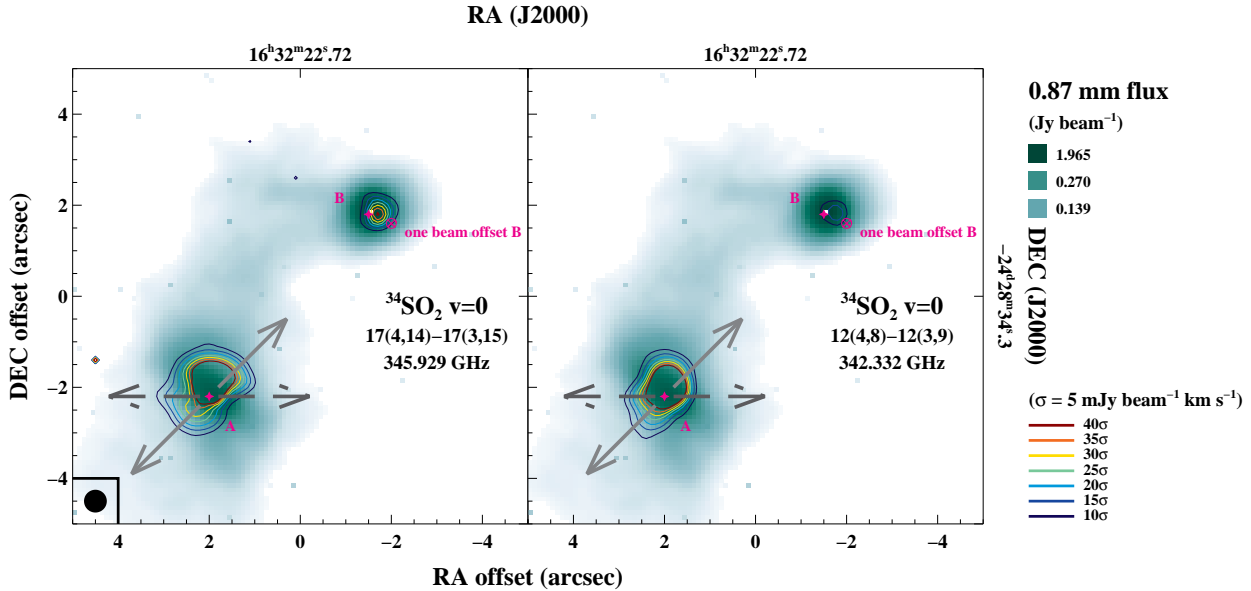


Figure 1. Integrated intensity maps of two transition of $^{34}\text{SO}_2$, see Section 3.8 for details. The centre of the pixel of the one beam offset position from IRAS 16293–2422 B corresponds to (RA, Dec) J2000 = ($16^{\text{h}}32^{\text{m}}22^{\text{s}}.58$, $-24^{\circ}28'32''.80$). The directions of the outflows are indicated with the arrows.

(Fig. B2). Integrating over 9 spectral bins yields the total flux of this line at the one beam offset position of $\sim 26 \text{ mJy beam}^{-1} \text{ km s}^{-1}$. The total flux of this line integrated over the entirety of source B (Fig. 1) is $\sim 150 \text{ mJy km s}^{-1}$ (for $\text{RA} \in [-1''.0, -2''.4]$ and $\text{Dec} \in [1''.3, 2''.2]$). Taking the ratio of these two numbers implies that ~ 17 per cent of the total 342 GHz line emission of $^{34}\text{SO}_2$ towards source B is picked up in a beam solid angle at the one beam offset position. For the purposes of this paper, which are to compare and contrast the chemical composition of the smallest discscales around source B to those of comet 67P/C-G, it has been chosen to focus on this single position rather than the entire emitting area (which also differs per molecule). Emission from other species, such as CS and its isotopologues, is likely a superposition of extended (envelope) and the more compact (disc) components. However, these ALMA observations are marginally sensitive to envelope emission, since any structure that is smooth on scales of more than $\sim 13''$ is filtered, even by the ACA.

4 DISCUSSION

4.1 Comparison with single dish observations

The presented interferometric observations spatially resolve the hot inner regions near the source B continuum peak, meaning that column densities can be derived and compared on the same scales unambiguously. Moreover, it is possible to detect weaker lines from multiple isotopologues, thereby allowing a better determination of the optical depth. By comparing molecular ratios of interferometric and single dish observations, it is possible to disentangle whether molecules primarily emit on large scales or small inner scales near the source, or whether they are associated with outflows. For this purpose, Table 3 has been compiled with molecular ratios of the detected species relative to H_2S and OCS (where available), as obtained with the PILS survey with ALMA at the one beam offset position and as compiled from previous single dish observations

of Schöier et al. (2002). Since single dish observations cannot spatially resolve the emission, three different sets of abundances are typically provided: one assuming a constant abundance profile and one assuming a jump abundance profile, giving an inner (hot) abundance and an outer (cold) one.

Under the assumption of a constant abundance profile, relative to H_2S , the interferometric ratios are lower than those from single dish observations: by a factor of 3 – 30 for OCS, by 3 – 4 orders of magnitude for SO, and by 2 – 3 orders of magnitude for SO_2 , CS, and H_2CS (Table 3). Relative to OCS, the interferometric ratio is a factor of 3 – 30 higher than the single dish value for H_2S . All other interferometric ratios remain lower than the single dish: by 2 orders of magnitude for SO, by a factor of ~ 18 for SO_2 , by a factor of ~ 27 for CS and by a factor of ~ 6 for H_2CS . Under the assumption of a jump abundance profile, relative to OCS, the differences are either comparable or exacerbated further. The inner ratio is expected to yield the most meaningful comparison with interferometric data, as it is the closest estimate for the hot inner regions studied in this work.

The derived lower interferometric ratios mean that sulphur-bearing species emit on small and large scales. Single dish observations are, therefore, a combination of beam-diluted disc-scale emission (isotopologues detected) and large-scales emission from the envelope and outflows. The largest differences are seen for SO, which is a well-known shock tracer that shows larger line widths in the single dish data (Blake et al. 1994). Some SO_2 emission likely originates from outflows as well. Meanwhile, OCS, H_2S and H_2CS emit also from the envelope. In fact, H_2CS is one of the few species detected at large distances from source A (appendices C1 and C2 of Murillo et al. 2017), definitively pointing to its origins in the extended envelope. However, the detection of all these molecules with interferometric data testifies to their presence on small scales of the disc and/or inner envelope as well. Unfortunately, it is not meaningful to quantify these differences, since single dish observations also encompass source A. The emission from sulphur-bearing species is

Table 3. Molecular ratios relative to H₂S and OCS as measured with PILS interferometric ALMA observations at the one beam offset position from source B of IRAS 16293–2422 and with previous single dish (SD) work^m

| Species | N (cm ⁻²) | Molecular ratios relative to H ₂ S (%) | | Molecular ratios relative to OCS (%) | | | |
|-------------------|-------------------------------|---|-------------|--------------------------------------|-------------|----------|----------|
| | | ALMA B | SD constant | ALMA B | SD constant | SD inner | SD outer |
| H ₂ S | 1.9 × 10 ^{17,i-18,j} | 100 | 100 | 68 – 679 | 23 | - | - |
| OCS | 2.8 × 10 ¹⁷ | 147 – 15 | 438 | 100 | 100 | 100 | 100 |
| SO | 5.0 × 10 ¹⁴ | 0.3 – 0.03 | 275 | 0.2 | 63 | 100 | 117 |
| SO ₂ | 1.5 × 10 ¹⁵ | 0.8 – 0.08 | 39 | 0.5 | 9 | 40 | 15 |
| CS | 4.4 × 10 ¹⁵ | 2 – 0.2 | 188 | 2 | 43 | - | - |
| H ₂ CS | 1.5 × 10 ¹⁵ | 0.8 | 13 | 0.5 | 3 | 1 | 3 |

^m tables 5 and 6 of Schöier et al. (2002)

Table 4. Molecular ratios relative to H₂S and OCS as measured with these interferometric ALMA observations at the one beam offset position from source B of IRAS 16293–2422 in comparison to those of 67P/C–Gⁿ and ISM ices towards W33A^o

| Species | N (cm ⁻²) | Molecular ratios relative to H ₂ S (%) | | Molecular ratios relative to OCS (%) | | |
|----------------------------------|-------------------------------|---|----------------|--------------------------------------|---------|---------------|
| | | ALMA B | 67P/C–G | ALMA B | 67P/C–G | ISM ices W33A |
| H ₂ S | 1.9 × 10 ^{17,i-18,j} | 100 | 100 | 68 – 679 | 2257 | < 30 – 90 |
| OCS | 2.8 × 10 ¹⁷ | 147 – 15 | 4.43 ± 0.15 | 100 | 100 | 100 |
| SO | 5.0 × 10 ¹⁴ | 0.3 – 0.03 | 7.06 ± 0.17 | 0.2 | 159 | - |
| SO ₂ | 1.5 × 10 ¹⁵ | 0.8 – 0.08 | 12.5 ± 0.3 | 0.5 | 282 | 3 – 7 |
| S ₂ | ≤ 2.2 × 10 ¹⁶ | ≤ 12 | 0.25 ± 0.05 | ≤ 8 | 6 | - |
| S ₃ | ≤ 4.0 × 10 ¹⁵ | ≤ 2 | ~ 1 | ≤ 1 | ~ 23 | - |
| HS ₂ | ≤ 5.0 × 10 ¹⁴ | ≤ 0.3 | ≤ 0.01 | ≤ 0.2 | ≤ 0.2 | - |
| H ₂ S ₂ | ≤ 9.0 × 10 ¹⁴ | ≤ 0.5 | ≤ 0.057 | ≤ 0.3 | ≤ 1 | - |
| H ₂ CS | 1.5 × 10 ¹⁵ | 0.8 | 2.25 ± 1.38 | 0.5 | 51 | - |
| CH ₃ SH | 5.5 × 10 ¹⁵ | 3 – 0.3 | 3.5 ± 1.0 | 2 | 79 | - |
| C ₂ H ₅ SH | ≤ 1.8 × 10 ^{15,p} | ≤ 0.9 | 0.0338 ± 0.018 | ≤ 0.6 | 0.08 | - |

ⁿ see Section 4.3 for the details on the ROSINA data

^o ice ratios in the cold outer protostellar envelope of the high-mass protostar W33A, which are assumed to be representative of ISM ices (Boogert et al. 1997; van der Tak et al. 2003)

^p using the average of the upper limits on the column densities of gauche-C₂H₅SH and anti-C₂H₅SH

seen to be brighter towards source A, which may correlate with A powering stronger outflows. It is beyond the scope of this work to quantify the individual contributions of the two sources in single dish observations.

4.2 Comparison with interstellar ices

The interstellar ices in clouds and cores prior to the onset of star formation (i.e., prestellar ices) can only be observed in absorption against a bright background source. Observations towards the high-mass protostar W33A also show deep absorption features corresponding to ices in a protostellar envelope, which are water-dominated, but also contain trace species, including CH₃OH (Boogert et al. 1997; van der Tak et al. 2003). The ices in the outer cold protostellar envelope have been suggested to be chemically representative of prestellar ices (just prior to star formation) based on observations of non-sulphur bearing molecules (Boogert, Gerakines & Whittet 2015). Table 4 contains the ice molecular ratios relative to OCS as observed towards W33A in its outer cold protostellar envelope and are assumed to be representative of ISM ices, thus called as such. It is interesting to compare ISM ices to the warm (> 100 K) gas near the forming B protostar of IRAS 16293–2422 to assess the degree of processing between the cold outer protostellar envelope ices and this earliest warm embedded protostellar phase; assuming that the ices have just

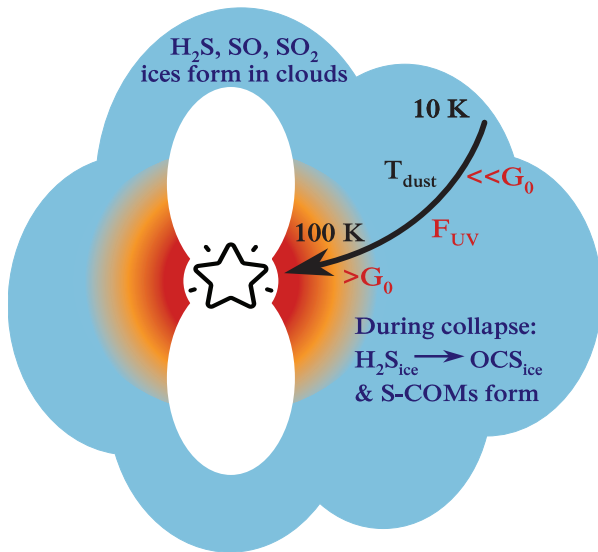
thermally desorbed, and no gas-phase chemistry has occurred. The ISM SO₂/OCS ratio is roughly an order of magnitude higher, which means that in the cold outer protostellar envelope there is more SO₂ or less OCS in comparison to the warm protostellar phase of IRAS 16293–2422 B. The H₂S/OCS ratio is poorly constrained due to a lack of data on H₂S ice and gas. Based on the current limits, the ISM ratio can be lower (by an order of magnitude) or higher (by a factor of ~ 1.3) than that of source B. If the ISM H₂S/OCS is indeed higher than that towards source B, then there may indeed be less OCS in the cold outer protostellar envelope than in the warm protostellar phase.

4.3 Comparison with 67P/C–G and ISM ices

IRAS 16293–2422 is thought to be analogous to our innate Solar Nebula, as it is one of the most chemically rich low-mass protostellar systems. Thanks to its proximity and the face-on orientation of the disc around source B, ALMA has been able to start precisely quantifying the chemistry of the disc-neighbourhood of B. Meanwhile, it has also been postulated that comets are the most pristine tracers of the innate cloud and protoplanetary disc that evolved into the Solar System that we have today. Therefore, it is interesting to compare the chemical inventories of comets to those of IRAS 16293–2422 B in order to quantify the chemical budgets of solar and extrasolar building blocks of planetary systems

Table 5. Molecular ratios as measured with these interferometric ALMA observations at the one beam offset position from source B of IRAS 16293–2422 and with the ROSINA instrument for 67P/C–G^a

| Ratio | ALMA B | 67P/C–G |
|---|---------------------|---|
| SO/SO ₂ | 0.33 | 0.4 – 0.7 (section 4.4 of Calmonte et al. 2016) |
| CH ₃ SH/H ₂ CS | 3.7 | 0.69 – 5.2 (based on values in Table 4) |
| C ₂ H ₅ SH/CH ₃ SH | ≤ 0.33 ^p | 0.0010 – 0.021 (based on values in Table 4) |

**Figure 2.** A schematic summarizing the chemical evolution of S-bearing species during the earliest phases of low-mass star formation. S-COMs stands for S-bearing complex organic molecules. G_0 is the interstellar FUV radiation field of $1.6 \times 10^{-3} \text{ erg cm}^{-2} \text{ s}^{-1}$ (Habing 1968).

(Schöier et al. 2002; Bockelée-Morvan et al. 2015). The emission seen in the hot inner regions of the B protostellar core could potentially be tracing solid species that are just undergoing thermal desorption and thus, is in fact probing the hidden solid reservoir of planet-building material. The chemical composition of such building blocks will be shaped by many processes at different radii; however, this location likely uniquely probes the solid volatiles prior to modification in the gas-phase.

Table 4 contains the molecular ratios relative to H₂S and OCS for IRAS 16293–2422 B in comparison to those of 67P/C–G. The cometary values correspond to bulk coma quantities measured with DFMS/ROSINA and corrected for photodissociation and ionization by the radiation from the Sun (more important when in high proximity to the Sun and when the comet-spacecraft distance is large, e.g., $\sim 200 \text{ km}$; table 3 of Calmonte et al. 2016), as obtained between equinox in May 2015 and perihelion in August 2015 (heliocentric distances between 1 and 2 au). The upper limits for HS₂ and H₂S₂ are based on October 2014 data, when H₂S abundance was maximized (sections 4.1.3 and 4.3.5 of Calmonte et al. 2016). The value given for S₃ is an estimate based on the sole measurement obtained in March 2015 via a direct comparison of the measured ion current (largely uncertain, section 4.1.2 of Calmonte et al. 2016). The value tabulated for H₂CS is based upon the sole clear signal at 46 u/e during a flyby in February 2015, when the CO₂ abundance was very low and the overlap with C¹⁶O¹⁸O could be avoided (priv. comm. and section 4.2.3 of Calmonte et al. 2016). The value

quoted for CH₃SH is the mean of the four periods between the start of the mission and perihelion with a signal at 48 u/e corrected for photodissociation and ionization (section 4.3.4 of Calmonte et al. 2016). The value quoted for C₂H₅SH is the mean of four different periods between the start of the mission and perihelion with a signal at 62 u/e not corrected for photodissociation and ionization (sections 4.1.1 and 4.3.4 of Calmonte et al. 2016), which is highly uncertain due to the assumption of the entire C₂H₆S peak being associated with ethyl mercaptan and the close overlap with the C₅H₂ fragment. The errors in Table 4 for the DFMS/ROSINA measurements stem from instrumental uncertainties (section 3.3 of Calmonte et al. 2016).

From the table, it can be seen that for OCS the ratio relative to H₂S for IRAS 16293–2422 B is a factor of 3 \sim 33 higher than that for 67P/C–G, for SO a factor of 2 \sim 24 lower, for SO₂ a factor of 2 \sim 16 lower and for CH₃SH a factor of 1.2 \sim 12 lower⁵. Relative to OCS, the IRAS 16293–2422 B ratios for SO and SO₂ are \sim 3 orders of magnitude lower, and for CH₃SH is \sim 1 order of magnitude lower. Such large differences are consistent with the fact that H₂S has not yet been detected in interstellar ices, but OCS has (Section 4.2).

These results indicate that in the case of IRAS 16293–2422 B there is significantly more OCS available, while for 67P/C–G more H₂S is present. Potentially, this has to do with the amount of solid carbon monoxide (CO) available in these systems. OCS may be more easily produced via grain-surface chemistry when CO ice is abundant, as seen in laboratory experiments of Ferrante et al. (2008). If so, then once CO undergoes thermal desorption into the gas-phase around 20 K, the production of OCS would be inhibited (excluding any CO that maybe trapped in other ices). This could be an initial indication of our Solar System being born in a somewhat warmer, $> 20 \text{ K}$, environment rather than in the 10 – 15 K regime, which would lead to a deficiency of CO ice on the grains for the synthesis of OCS. This scenario is also favoured from the point of view of oxygen chemistry and the detection of O₂ on 67P/C–G (Bieler et al. 2015; Taquet et al. 2016). In the case of IRAS 16293–2422 B, observations have shown its surrounding core to be very cold ($\sim 12 \text{ K}$; Menten et al. 1987), thus making CO ice plentiful in its birth cloud. It has been suggested that regions with elevated temperatures lead to CO ice-poor conditions, for example, the R CrA region with several low-mass protostars under the irradiation of an intermediate-mass protostar (Lindberg et al. 2014), and Orion hosting intermediate-mass protostars (Jørgensen et al. 2006).

A warmer environment would imply less efficient hydrogenation reactions, as the residence time of hydrogen atoms on the grains is reduced. This would make it difficult to produce H₂S through grain-surface atom-addition reactions. This molecule is

⁵ This contradicts section 5.2 of Calmonte et al. (2016) due to different assumptions on the quantity of H₂S and the use of abundances versus column densities.

predominantly formed via the associations of H and S, followed by the reaction of HS with H (e.g. Furuya et al. 2015; Vidal et al. 2017). Some H₂S gas can also be produced via gas-phase channels at warmer temperatures. Temperature differences between birth clouds should also be noticeable in terms of complex organics. An initially warmer cloud would enhance mobility of heavy radicals on grain surfaces, such as CH₃ and SH, thereby boosting the abundance of complex species, such as CH₃SH (although it is not exclusively formed via grain-surface chemistry). The CH₃SH/H₂CS ratio for IRAS 16293–2422 B is in range of the ratio for 67P/C–G given the errors in ROSINA data (differences by a factor of 0.7 – 5.3; Table 5). Hence, based the complex S-bearing species CH₃SH relative to H₂CS, it is not possible to conclusively say which target is richer in complex organic molecules. Given the large differences in the quantities of H₂S and OCS between the two data sets, ratios relative to them are less meaningful. As it has only been possible to derive an upper limit for C₂H₅SH, the C₂H₅SH/CH₃SH ratio cannot yet be used to compare the budgets of S-bearing complex species between IRAS 16293–2422 B and 67P/C–G. A rigorous comparison between IRAS 16293–2422 B and 67P/C–G in terms of a larger set of other O- and N-bearing complex organics is the subject of a dedicated paper.

Additional physics could be at play here - the degree of irradiation that the two targets are subjected to. Our Sun is an isolated star that is thought to have formed in a medium-sized stellar cluster of 10³ – 10⁴ members (Adams 2010). Laboratory experiments of Chen et al. (2015) have shown rapid conversion of H₂S into OCS upon VUV and EUV irradiation. If IRAS 16293–2422 B experienced higher UV fluxes, perhaps due to its binary A companion, then that may have stimulated the conversion of its H₂S reservoir into OCS. In addition, higher levels of UV would explain the higher fraction of complex S-bearing species relative to H₂CS of IRAS 16293–2422 B, since UV enhances the availability of radicals in the ice and boosts grain-surface chemistry. This scenario would also correlate with OCS forming during the collapse phases and there, thus, being less OCS in ISM ices (Section 4.2; although, the presence of H₂S ice is yet to be demonstrated and quantified in prestellar sources).

Another diagnostic independent of the H₂S and OCS quantities, is the SO/SO₂ ratio. Based on the presented PILS Band 7 data, it is 0.33 for IRAS 16293–2422 B; and based on the ROSINA data, it is in the 0.4 – 0.7 range for 67P/C–G (Table 5). Such excellent (a factor of ~ 2) agreement could point to both datasets sampling comparable materials. If the quantities of SO and SO₂ are set before and/or during the prestellar stage, as supported by the detection of SO₂ as an ISM ice (Section 4.2), then this again points to IRAS 16293–2422 B and 67P/C–G having formed from similar birth clouds. Unfortunately, even with JWST it may be impossible to quantify the ISM SO/SO₂ ice ratio due to the overlap of their symmetric stretching modes. Gas-phase routes to SO and SO₂ via reactions of OH and O₂ with S at warm temperatures may also skew the ratio.

The ROSINA instrument determined that ~ 27 per cent of the sulphur is in the atomic form and constitutes the second largest sulphur reservoir after H₂S (fig. 16 of Calmonte et al. 2016). It was also argued that five times more H₂S than detected would be necessary to account for the measured quantity of atomic sulphur, hence it is indeed stored in its atomic form in 67P/C–G (Calmonte et al. 2016). Unfortunately, atomic sulphur does not have any lines in the frequency range covered by the PILS Band 7 data. 67P/C–G has been observed to contain sulphur-chain molecules like S₂, S₃ and S₄, which could, in part, be fragments of even heavier S_n

species (up to $n = 8$). The upper limits derived in this work are less constraining than the quantities measured for 67P/C–G (Table 4). ROSINA did not (conclusively) detect HS₂ and H₂S₂ (section 4.1.3 of Calmonte et al. 2016). These species were not detected towards IRAS 16293–2422 B with the PILS Band 7 data either. It was not possible to derive the abundance of CS with ROSINA, due to interference with CO₂; and due to it being a common fragment of other sulphur-bearing species. Hence, it cannot be compared in a meaningful fashion with the data in this work. Finally, as CS₂ is a linear symmetric molecule without strong rotational lines, it is not possible to search for it in the PILS Band 7 data; even though it has been clearly detected with mass spectrometry on 67P/C–G.

The findings of this work can be summarized in Fig. 2. It seems that the abundances of SO, SO₂ and H₂S are set in the translucent cloud and prestellar core phases, prior to the onset of collapse. This is supported by the similar relative ratios between the PILS data on IRAS 16293–2422 B, the ISM ices towards W33A (Section 4.2) and the ROSINA data on 67P/C–G. The differences between the datasets can be explained in terms of the amount of UV radiation that the materials are exposed to, which occurs during the collapse of the system, already in the earliest embedded stages, as well as the temperature of the birth cloud. Irradiation brings about the conversion of H₂S into OCS and the formation of S-bearing complex organic molecules. This explains the richer chemistry towards IRAS 16293–2422 B and our Solar System, in comparison to cold outer protostellar envelopes. Whether IRAS 16293–2422 B is relatively chemically richer than our Solar System as a result of higher UV fluxes based on its binary nature still remains to be conclusively tested via a larger set of complex organic species. If this is shown to be the case, then this would correlate with IRAS 16293–2422 being one of the most chemically rich low-mass protostars; and imply that our Solar System is not special chemically speaking.

5 CONCLUSIONS

In this paper, the sulphur inventory at the one beam offset position from source B in the SW direction in the binary protostellar system IRAS 16293–2422 has been presented. The ALMA Band 7 data analysed are part of the PILS survey towards this target. Sulphur is thought to be a unique simultaneous tracer of both the volatile and refractory components. By comparing molecular ratios observed towards IRAS 16293–2422 B – a Solar System proxy, and those obtained for 67P/C–G – a pristine tracer of the innate Solar Nebula, the chemical links between the early embedded protostellar phases and the protoplanetary building blocks can be explored. The main conclusions of this paper are as follows.

(i) The sulphur-bearing species previously detected towards IRAS 16293–2422 B have now been firmly detected towards the one beam offset position and spatially resolved with ALMA: SO₂ in the $\nu = 0$, ³⁴SO₂, OCS in the $\nu_2 = 1$ state, O¹³CS, OC³⁴S, OC³³S (first-time detection towards this source), ¹⁸OCS, H₂CS, HD₂CS and CH₃SH in the $\nu = 0 - 2$ state. Furthermore, several are detected tentatively due to a lack of lines and/or blending: SO in the $\nu = 0$ state, OCS in the $\nu = 0$ state, C³⁴S in the $\nu = 0, 1$ state, C³³S in the $\nu = 0, 1$ state, C³⁶S (tentative first time detection towards a low-mass protostar), HDS and HD³⁴S. All the lines from these sulphur-bearing molecules are narrow (~ 1 km s⁻¹) and are probing the small disc-scales of source B. Unfortunately, the unknown HDS/H₂S ratio leaves the column density of H₂S uncertain by at least an order of magnitude.

(ii) In comparison to earlier single dish observations, the molecular ratios determined from interferometric data can be up to four orders of magnitude lower. On large scales, SO and SO₂ likely emit from outflows; and OCS, H₂S and H₂CS originate from the envelope. All these S-bearing species are also present on the small disc- and inner envelope-scales. Single dish data may be dominated by source A, which is bright in emission from S-bearing molecules.

(iii) In comparison to ROSINA measurements of the bulk volatile composition of 67P/C-G, the molecular ratios of IRAS 16293–2422 B can differ significantly, potentially by several orders of magnitude. In particular, IRAS 16293–2422 B contains much more OCS than H₂S. However, the SO/SO₂ is in close agreement between the two targets.

(iv) The agreement in terms of SO, SO₂, the disagreement in terms of H₂S and OCS, and comparable (differences by a factor of 0.7 – 5.3) CH₃SH/H₂CS ratios towards IRAS 16293–2422 B in comparison to that of our Solar System (as probed by 67P/C-G) may stem from different levels of UV irradiation during the initial collapse of the systems. Potentially higher UV levels near source B, as a result of its binary structure, may lead to the conversion of H₂S into OCS and enhance the formation of S-bearing complex organic molecules. An initially warmer birth cloud may also contribute to the lower quantities of OCS in the Solar System by reducing the amount of available CO ice.

The results also highlight the importance of the level of UV exposure and temperature of the parental clouds, in determining the physical and chemical structures of low-mass protostars. Given that these may vary significantly from region to region (see, e.g., review by Adams 2010), it is also likely that significant source-to-source variations in chemistry may be found. Future studies will also explore the protostellar-cometary connection via isotopic ratios and a full set of complex organic species, thereby isolating chemical links formed during cold phases of evolution that are dominated by grain-surface chemistry from those occurring during warmer, irradiated phases of collapse.

6 ACKNOWLEDGEMENTS

The authors would like to thank Dr. Catherine Walsh, Dr. Vianney Taquet, Mr. Ko-Ju Chuang and Dr. Martin Rubin for useful discussions on sulphur chemistry and ROSINA measurements. This work is supported by a Huygens fellowship from Leiden University, the European Union A-ERC grant 291141 CHEMPLAN, the Netherlands Research School for Astronomy (NOVA), a Royal Netherlands Academy of Arts and Sciences (KNAW) professor prize, the Center for Space and Habitability (CSH) Fellowship and the IAU Gruber Foundation Fellowship.

The research of JKJ and his group is supported by the European Research Council (ERC) under the European Union’s Horizon 2020 research and innovation programme (grant agreement No 646908) through ERC Consolidator Grant “S4F”. Research at the Centre for Star and Planet Formation is funded by the Danish National Research Foundation. A.C. postdoctoral grant is funded by the ERC Starting Grant 3DICE (grant agreement 336474).

This paper makes use of the following ALMA data: ADS/JAO.ALMA#2013.1.00278.S. ALMA is a partnership of ESO (representing its member states), NSF (USA) and NINS (Japan), together with NRC (Canada), MOST and ASIAA (Taiwan), and KASI (Republic of Korea), in cooperation with the Republic of Chile. The Joint ALMA Observatory is operated by ESO, AUI/NRAO and NAOJ.

REFERENCES

- Adams F. C., 2010, *ARA&A*, 48, 47
- A’Hearn M. F., Schleicher D. G., Feldman P. D., 1983, *ApJ*, 274, L99
- Ahrens V., Winnewisser G., 1999, *Zeitschrift Naturforschung Teil A*, 54, 131
- Aikawa Y. et al., 2012, *A&A*, 538, A57
- Altwegg K. et al., 2017, *MNRAS*, 469, S130
- Anderson D. E., Bergin E. A., Maret S., Wakelam V., 2013, *ApJ*, 779, 141
- Asplund M., Grevesse N., Sauval A. J., Scott P., 2009, *ARA&A*, 47, 481
- Balsiger H. et al., 2007, *Space Sci. Rev.*, 128, 745
- Baryshev A. M. et al., 2015, *A&A*, 577, A129
- Belloche A., Müller H. S. P., Menten K. M., Schilke P., Comito C., 2013, *A&A*, 559, A47
- Belov S. P., Tretyakov M. Y., Kozin I. N., Klisch E., Winnewisser G., Lafferty W. J., Flaud J.-M., 1998, *Journal of Molecular Spectroscopy*, 191, 17
- Belov S. P., Yamada K. M. T., Winnewisser G., Poteau L., Bocquet R., Demaison J., Polyansky O., Tretyakov M. Y., 1995, *Journal of Molecular Spectroscopy*, 173, 380
- Bettens F. L., Sastry K. V. L. N., Herbst E., Albert S., Oesterling L. C., De Lucia F. C., 1999, *ApJ*, 510, 789
- Bieler A. et al., 2015, *Nature*, 526, 678
- Biver N. et al., 2016, *A&A*, 589, A78
- Blake G. A., van Dishoeck E. F., Jansen D. J., Groesbeck T. D., Mundy L. G., 1994, *ApJ*, 428, 680
- Blake G. A., van Dishoeck E. F., Sargent A. I., 1992, *ApJ*, 391, L99
- Bockelée-Morvan D. et al., 2015, *A&A*, 583, A6
- Bogey M., Civiš S., Delcroix B., Demuyneck C., Krupnov A. F., Quiguer J., Tretyakov M. Y., Walters A., 1997, *Journal of Molecular Spectroscopy*, 182, 85
- Bogey M., Demuyneck C., Destombes J. L., 1982, *Journal of Molecular Spectroscopy*, 95, 35
- Boogert A. C. A., Gerakines P. A., Whittet D. C. B., 2015, *ARA&A*, 53, 541
- Boogert A. C. A., Schutte W. A., Helmich F. P., Tielens A. G. G. M., Wooden D. H., 1997, *A&A*, 317, 929
- Calmonte U. et al., 2016, *MNRAS*, 462, S253
- Calmonte U. et al., 2017, *Monthly Notices of the Royal Astronomical Society*, stx2534
- Camy-Peyret C., Flaud J.-M., Lechuga-Fossat L., Johns J. W. C., 1985, *Journal of Molecular Spectroscopy*, 109, 300
- Caux E. et al., 2011, *A&A*, 532, A23
- Cernicharo J., Marcelino N., Roueff E., Gerin M., Jiménez-Escobar A., Muñoz Caro G. M., 2012, *ApJ*, 759, L43
- Chen Y.-J. et al., 2015, *ApJ*, 798, 80
- Coutens A. et al., 2016, *A&A*, 590, L6
- Drdla K., Knapp G. R., van Dishoeck E. F., 1989, *ApJ*, 345, 815
- Dubrulle A., Demaison J., Burie J., Boucher D., 1980, *Zeitschrift Naturforschung Teil A*, 35, 471
- Duley W. W., Millar T. J., Williams D. A., 1980, *MNRAS*, 192, 945
- Esplugues G. B., Viti S., Goicoechea J. R., Cernicharo J., 2014, *A&A*, 567, A95
- Fabricant B., Krieger D., Muentner J. S., 1977, *J. Chem. Phys.*, 67, 1576
- Ferrante R. F., Moore M. H., Spiliotis M. M., Hudson R. L., 2008, *ApJ*, 684, 1210
- Furuya K., Aikawa Y., Hincelin U., Hassel G. E., Bergin E. A., Vasyunin A. I., Herbst E., 2015, *A&A*, 584, A124
- Geiss J., 1988, in *Reviews in Modern Astronomy*, Vol. 1, *Reviews in Modern Astronomy*, Klare G., ed., pp. 1–27
- Gibb E. L. et al., 2000, *ApJ*, 536, 347
- Glassmeier K.-H., Boehnhardt H., Koschny D., Kürt E., Richter I., 2007, *Space Sci. Rev.*, 128, 1
- Goesmann F. et al., 2015, *Science*, 349, 020689
- Goicoechea J. R., Pety J., Gerin M., Teyssier D., Roueff E., Hily-Blant P., Baek S., 2006, *A&A*, 456, 565
- Golubiatnikov G. Y., Lapinov A. V., Guarnieri A., Knöchel R., 2005, *Journal of Molecular Spectroscopy*, 234, 190
- Grim R. J. A., Greenberg J. M., 1987, *A&A*, 181, 155
- Habing H. J., 1968, *Bull. Astr. Inst. Neth.*, 19, 421
- Hasegawa T. et al., 1984, *ApJ*, 283, 117
- Helminger P., Cook R. L., De Lucia F. C., 1971, *Journal of Molecular Spectroscopy*, 40, 125
- Hillger R. E., Strandberg M. W., 1951, *Physical Review*, 83, 575
- Hirahara Y. et al., 1992, *ApJ*, 394, 539
- Jansen D. J., van Dishoeck E. F., Black J. H., 1994, *A&A*, 282, 605
- Jefferts K. B., Penzias A. A., Wilson R. W., Solomon P. M., 1971, *ApJ*, 168, L111
- Jessberger E. K., Christoforidis A., Kissel J., 1988, *Nature*, 332, 691
- Jessup K. L., Spencer J., Yelle R., 2007, *Icarus*, 192, 24
- Jørgensen J. K., Bourke T. L., Nguyen Luong Q., Takakuwa S., 2011, *A&A*, 534, A100
- Jørgensen J. K., Favre C., Bisschop S. E., Bourke T. L., van Dishoeck E. F., Schmalzl M., 2012, *ApJ*, 757, L4
- Jørgensen J. K., Johnstone D., van Dishoeck E. F., Doty S. D., 2006, *A&A*, 449, 609
- Jørgensen J. K. et al., 2017, *A&A*, *subm.*
- Jørgensen J. K. et al., 2016, *A&A*, 595, A117
- Kolesníková L., Tercero B., Cernicharo J., Alonso J. L., Daly A. M., Gordon B. P., Shipman S. T., 2014, *ApJ*, 784, L7
- Le Roy L. et al., 2015, *A&A*, 583, A1
- Leen T. M., Graff M. M., 1988, *ApJ*, 325, 411
- Ligterink N. F. W. et al., 2017, *MNRAS*, 469, 2219
- Lindberg J. E., Jørgensen J. K., Green J. D., Herczeg G. J., Dionatos O., Evans N. J., Karska A., Wampfler S. F., 2014, *A&A*, 565, A29
- Linke R. A., Frerking M. A., Thaddeus P., 1979, *ApJ*, 234, L139
- Loinard L., Torres R. M., Mioduszewski A. J., Rodríguez L. F., 2008, *ApJ*, 675, L29
- Lucas R., Liszt H. S., 2002, *A&A*, 384, 1054
- Lykke J. M. et al., 2017, *A&A*, 597, A53
- Maeda A. et al., 2008, *ApJS*, 176, 543
- Majumdar L., Gratier P., Vidal T., Wakelam V., Loison J.-C., Hickson K. M., Caux E., 2016, *MNRAS*, 458, 1859
- Martín-Doménech R., Jiménez-Serra I., Muñoz Caro G. M., Müller H. S. P., Occhiogrosso A., Testi L., Woods P. M., Viti S., 2016, *A&A*, 585, A112
- Mauersberger R., Henkel C., Langer N., Chin Y.-N., 1996, *A&A*, 313, L1
- Menten K. M., Serabyn E., Guesten R., Wilson T. L., 1987, *A&A*, 177, L57
- Millar T. J., Herbst E., 1990, *A&A*, 231, 466
- Minh Y. C., Irvine W. M., McGonagle D., Ziurys L. M., 1990, *ApJ*, 360, 136
- Minowa H., Satake M., Hirota T., Yamamoto S., Ohishi M., Kaifu N., 1997, *ApJ*, 491, L63

- Mitchell G. F., 1984, *ApJ*, 287, 665
- Morino I., Yamada K. M. T., Maki A. G., 2000, *Journal of Molecular Spectroscopy*, 200, 145
- Mouillet A., Lellouch E., Moreno R., Gurwell M., Black J. H., Butler B., 2013, *ApJ*, 776, 32
- Mouillet A., Lellouch E., Moreno R., Gurwell M. A., Moore C., 2008, *A&A*, 482, 279
- Müller H. S. P. et al., 2016, *A&A*, 587, A92
- Müller H. S. P., Brünken S., 2005, *Journal of Molecular Spectroscopy*, 232, 213
- Müller H. S. P., Schlöder F., Stutzki J., Winnewisser G., 2005, *Journal of Molecular Structure*, 742, 215
- Mumma M. J., Charnley S. B., 2011, *ARA&A*, 49, 471
- Murillo N. M., van Dishoeck E. F., van der Wiel M. H. D., Jørgensen J. K., Drozdovskaya M. N., Calcutt H., Harsono D., 2017, *A&A*, under rev.
- Oppenheimer M., Dalgarno A., 1974, *ApJ*, 187, 231
- Ortiz-León G. N. et al., 2017, *ApJ*, 834, 141
- Oya Y., Sakai N., López-Sepulcre A., Watanabe Y., Ceccarelli C., Lefloch B., Favre C., Yamamoto S., 2016, *ApJ*, 824, 88
- Palumbo M. E., Geballe T. R., Tielens A. G. G. M., 1997, *ApJ*, 479, 839
- Palumbo M. E., Tielens A. G. G. M., Tokunaga A. T., 1995, *ApJ*, 449, 674
- Pastor J., Buj J., Estalella R., Lopez R., Anglada G., Planesas P., 1991, *A&A*, 252, 320
- Patel D., Margolese D., Dyke T. R., 1979, *J. Chem. Phys.*, 70, 2740
- Penzias A. A., Solomon P. M., Wilson R. W., Jefferts K. B., 1971, *ApJ*, 168, L53
- Persson M. V. et al., 2017, *A&A*, accep.
- Pineau des Forets G., Roueff E., Flower D. R., 1986, *MNRAS*, 223, 743
- Pineda J. E. et al., 2012, *A&A*, 544, L7
- Powell F. X., Lide, Jr. D. R., 1964, *J. Chem. Phys.*, 41, 1413
- Prasad S. S., Huntress, Jr. W. T., 1982, *ApJ*, 260, 590
- Rotundi A. et al., 2015, *Science*, 347, aaa3905
- Ruffle D. P., Hartquist T. W., Caselli P., Williams D. A., 1999, *MNRAS*, 306, 691
- Sakai N. et al., 2014, *Nature*, 507, 78
- Schöier F. L., Jørgensen J. K., van Dishoeck E. F., Blake G. A., 2002, *A&A*, 390, 1001
- Smith D., Adams N. G., Giles K., Herbst E., 1988, *A&A*, 200, 191
- Tanaka K., Tanaka T., Suzuki I., 1985, *J. Chem. Phys.*, 82, 2835
- Taquet V., Furuya K., Walsh C., van Dishoeck E. F., 2016, *MNRAS*, 462, S99
- Tsunekawa S., Taniguchi I., Tambo A., Nagai T., Kojima T., Nakagawa K., 1989, *Journal of Molecular Spectroscopy*, 134, 63
- Turner B. E., 1992, *ApJ*, 396, L107
- van der Tak F. F. S., Boonman A. M. S., Braakman R., van Dishoeck E. F., 2003, *A&A*, 412, 133
- van Dishoeck E. F., Blake G. A., Jansen D. J., Groesbeck T. D., 1995, *ApJ*, 447, 760
- Vidal T. H. G., Loison J.-C., Jaziri A. Y., Ruaud M., Gratier P., Wakelam V., 2017, *MNRAS*, 469, 435
- Viswanathan R., Dyke T. R., 1984, *Journal of Molecular Spectroscopy*, 103, 231
- Watt G. D., Charnley S. B., 1985, *MNRAS*, 213, 157
- Wilson T. L., 1999, *Reports on Progress in Physics*, 62, 143
- Wilson T. L., Rood R., 1994, *ARA&A*, 32, 191
- Winnewisser G., Cook R. L., 1968, *Journal of Molecular Spectroscopy*, 28, 266
- Wlodek S., Bohme D. K., Herbst E., 1988, *MNRAS*, 235, 493
- Woods P. M., Occhiogrosso A., Viti S., Kaňuchová Z., Palumbo M. E., Price S. D., 2015, *MNRAS*, 450, 1256
- Xu L.-H. et al., 2012, *J. Chem. Phys.*, 137, 104313
- Zapata L. A., Palau A., Galván-Madrid R., Rodríguez L. F., Garay G., Moran J. M., Franco-Hernández R., 2015, *MNRAS*, 447, 1826

APPENDIX A: PARTITION OF SULPHUR ON 67P/C–G

For the moment, the data on elemental abundances in the dust of 67P/C–G has not been released by the Cometary Secondary Ion Mass Spectrometer (COSIMA) team. Therefore, the partition of sulphur between the refractory (dust) and volatile (ice) components has been derived based upon the information on the S/O ratio in volatiles as derived by the ROSINA team and the results obtained for comet 1P/Halley (Jessberger, Christoforidis & Kissel 1988).

For comet 1P/Halley, it has been shown that the dust to ice mass ratio is:

$$m_{\text{dust 1P}}/m_{\text{ice 1P}} = 2, \quad (\text{A1})$$

so then:

$$m_{\text{comet 1P}} = m_{\text{dust 1P}} + m_{\text{ice 1P}} = 3m_{\text{ice 1P}} = \frac{3}{2}m_{\text{dust 1P}}. \quad (\text{A2})$$

In other terms:

$$m_{\text{dust 1P}} = \frac{2}{3}m_{\text{comet 1P}} \quad (\text{A3})$$

and

$$m_{\text{ice 1P}} = \frac{1}{3}m_{\text{comet 1P}}. \quad (\text{A4})$$

According to Geiss (1988), 23 per cent of all the oxygen atoms on 1P/Halley is in the refractory (dust) component by number, i.e.:

$$n_{\text{O dust 1P}} = 0.23n_{\text{O tot 1P}}, \quad (\text{A5})$$

where n are total numbers of atoms and is dimensionless. So:

$$n_{\text{O ice 1P}} = 0.77n_{\text{O tot 1P}}. \quad (\text{A6})$$

Then the number densities (in cm^{-3}) of oxygen in the refractory (dust) and volatile (ice) components of 1P/Halley are given by:

$$\rho_{\text{O dust 1P}} = \frac{n_{\text{O dust 1P}}}{m_{\text{O dust 1P}}} \times P_{\text{O dust 1P}} = \frac{0.23n_{\text{O tot 1P}}}{\frac{2}{3}m_{\text{O comet 1P}}} \times P_{\text{O dust 1P}}, \quad (\text{A7})$$

$$\rho_{\text{O ice 1P}} = \frac{n_{\text{O ice 1P}}}{m_{\text{O ice 1P}}} \times P_{\text{O ice 1P}} = \frac{0.77n_{\text{O tot 1P}}}{\frac{1}{3}m_{\text{O comet 1P}}} \times P_{\text{O ice 1P}}, \quad (\text{A8})$$

where P are the mass densities (in g cm^{-3}). The ratio of the two is:

$$\rho_{\text{O ice 1P}}/\rho_{\text{O dust 1P}} = \frac{0.77 \times 2}{0.23} \times \frac{P_{\text{O ice 1P}}}{P_{\text{O dust 1P}}} \approx 6.7 \frac{P_{\text{O ice 1P}}}{P_{\text{O dust 1P}}}. \quad (\text{A9})$$

Now let us assume that 1P/Halley and 67P/C–G have been made from the same dust and ice. This means that $\rho_{\text{O ice 1P}} = \rho_{\text{O ice 67P}}$, $\rho_{\text{O dust 1P}} = \rho_{\text{O dust 67P}}$, and that $P_{\text{O ice 1P}} = P_{\text{O ice 67P}}$, $P_{\text{O dust 1P}} = P_{\text{O dust 67P}}$. Then it also follows that:

$$\rho_{\text{O ice 67P}}/\rho_{\text{O dust 67P}} \approx 6.7 \frac{P_{\text{O ice 67P}}}{P_{\text{O dust 67P}}}. \quad (\text{A10})$$

For comet 67P/C–G, Rotundi et al. (2015) derived that the dust to ice mass ratio is:

$$m_{\text{dust 67P}}/m_{\text{ice 67P}} = 4, \quad (\text{A11})$$

so then:

$$m_{\text{comet 67P}} = m_{\text{dust 67P}} + m_{\text{ice 67P}} = 5m_{\text{ice 67P}} = \frac{5}{4}m_{\text{dust 67P}}. \quad (\text{A12})$$

In other terms:

$$m_{\text{dust 67P}} = \frac{4}{5}m_{\text{comet 67P}} \quad (\text{A13})$$

and

$$m_{\text{ice 67P}} = \frac{1}{5}m_{\text{comet 67P}}. \quad (\text{A14})$$

Subsequently, the numbers of oxygen atoms in the refractory (dust) and volatile (ice) components of 67P/C–G become:

$$n_{\text{O dust 67P}} = \rho_{\text{O dust 67P}} \times \frac{m_{\text{O dust 67P}}}{P_{\text{O dust 67P}}} = \quad (\text{A15})$$

$$= \rho_{\text{O dust 67P}} \times \frac{\frac{4}{5}m_{\text{comet 67P}}}{P_{\text{O dust 67P}}}, \quad (\text{A16})$$

$$n_{\text{O ice 67P}} = \rho_{\text{O ice 67P}} \times \frac{m_{\text{O ice 67P}}}{P_{\text{O ice 67P}}} = \quad (\text{A17})$$

$$= \rho_{\text{O ice 67P}} \times \frac{\frac{1}{5}m_{\text{comet 67P}}}{P_{\text{O ice 67P}}}, \quad (\text{A18})$$

and the ratio of the two is:

$$n_{\text{O dust 67P}}/n_{\text{O ice 67P}} = 4 \times \frac{\rho_{\text{O dust 67P}}}{\rho_{\text{O ice 67P}}} \times \frac{P_{\text{O ice 67P}}}{P_{\text{O dust 67P}}} \approx \quad (\text{A19})$$

$$\approx 4 \times \frac{P_{\text{O dust 67P}}}{6.7 \times P_{\text{O ice 67P}}} \times \frac{P_{\text{O ice 67P}}}{P_{\text{O dust 67P}}} \approx 0.60. \quad (\text{A20})$$

Hence:

$$n_{\text{O comet 67P}} = n_{\text{O dust 67P}} + n_{\text{O ice 67P}} = 1.60n_{\text{O ice 67P}} = 2.7n_{\text{O dust 67P}}. \quad (\text{A21})$$

This implies that 37 per cent of all the oxygen atoms on 67P/C–G is in the refractory (dust) component by number; and that 63 per cent of all the oxygen atoms on 67P/C–G is in the volatile (ice) component by number.

It has also been shown by Jessberger, Christoforidis & Kissel (1988) that S/O in the dust of 1P/Halley is 8.1 per cent (based on values in table 1). Assuming again that 1P/Halley and 67P/C–G have been made from the same dust, i.e.:

$$(S/O)_{\text{dust 67P}} = (S/O)_{\text{dust 1P}} = 8.1\%; \quad (\text{A22})$$

then the overall S/O ratio in the dust and ice of 67P/C–G is:

$$(S/O)_{\text{comet 67P}} = \frac{n_{\text{O dust 67P}}}{n_{\text{O comet 67P}}} (S/O)_{\text{dust 67P}} + \frac{n_{\text{O ice 67P}}}{n_{\text{O comet 67P}}} (S/O)_{\text{ice 67P}} = \quad (\text{A23})$$

$$= 0.37 \times 8.1\% + 0.63 \times 1.47\% \approx 3.9\%,$$

where the S/O in the ice of 67P/C–G of 1.47 per cent has been used (as given in section 5.6 of Calmonte et al. 2016) as derived from ROSINA data.

If $(S/O)_{\text{comet 67P}} = 3.9\%$ and $(S/O)_{\text{ice 67P}} = 1.47\%$, then:

$$\frac{(S/O)_{\text{ice 67P}}}{(S/O)_{\text{comet 67P}}} = \frac{1.47}{3.9}, \quad (\text{A24})$$

$$\frac{n_{\text{S ice 67P}}}{n_{\text{S comet 67P}}} \times \frac{n_{\text{O comet 67P}}}{n_{\text{O ice 67P}}} = \frac{1.47}{3.9}, \quad (\text{A25})$$

$$\frac{n_{\text{S ice 67P}}}{n_{\text{S comet 67P}}} \times 1.6 = \frac{1.47}{3.9}, \quad (\text{A26})$$

$$\frac{n_{\text{S ice 67P}}}{n_{\text{S comet 67P}}} = \frac{1.47}{3.9 \times 1.6} = 0.24. \quad (\text{A27})$$

This means that 24 per cent of all the sulphur atoms on 67P/C–G are in the volatile (ice) component by number; and that 76 per cent of all the sulphur atoms on 67P/C–G are in the refractory (dust) component by number.

APPENDIX B: A SELECTION OF LINES AND SYNTHETIC SPECTRA OF S-BEARING SPECIES IN THE PILS BAND 7 DATASET

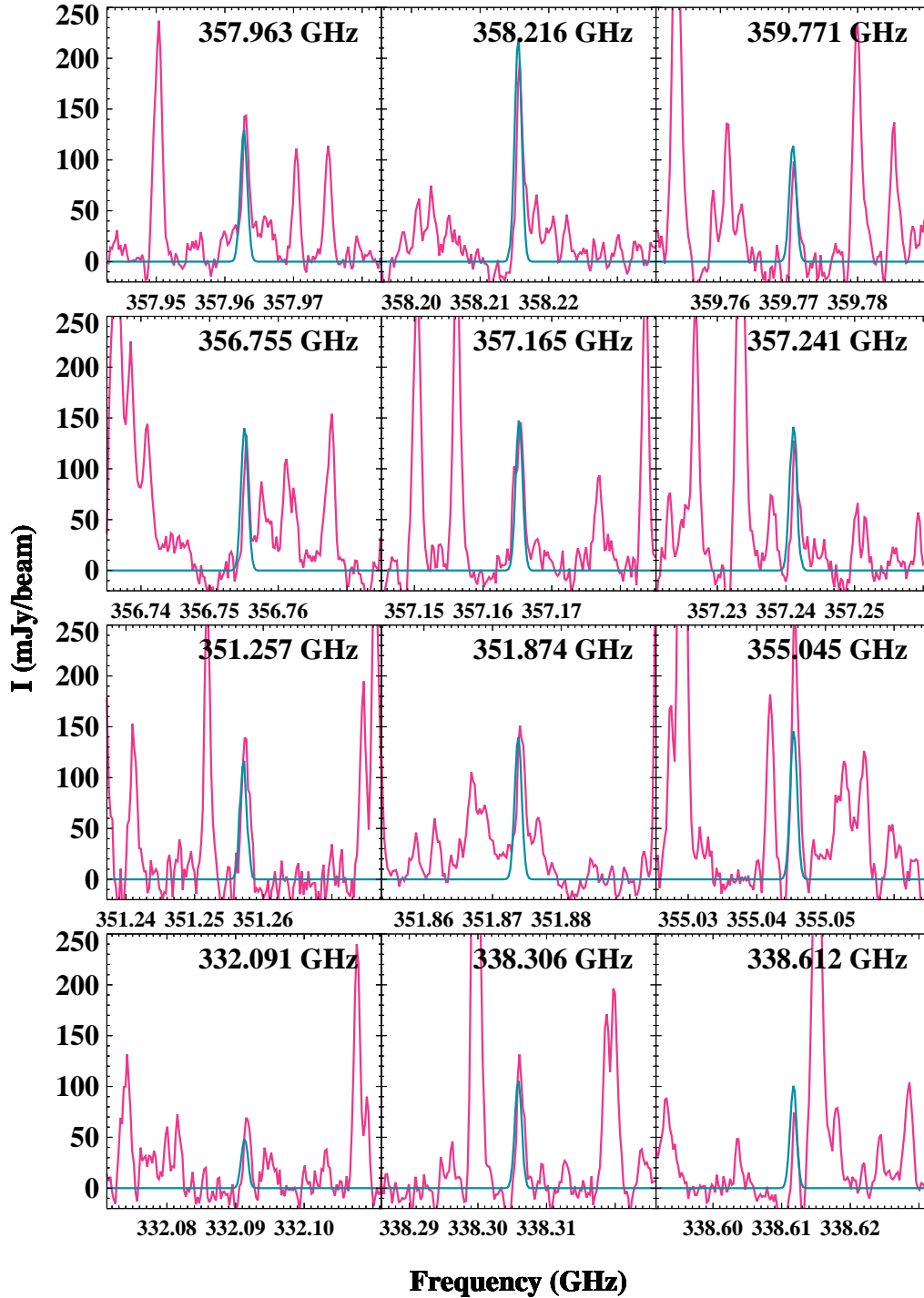


Figure B1. Twelve selected lines of SO_2 in the $\nu = 0$ state. The observed ALMA Band 7 spectrum convolved with a uniform circular restoring beam of $0''.5$ at the one beam (~ 60 au) offset from source B of IRAS 16293–2422 in the SW direction is in pink. The turquoise line is the LTE fit for each displayed transition, assuming a source size of $0''.5$, FWHM of 1 km s^{-1} , $T_{\text{ex}} = 125 \text{ K}$ and a column density as prescribed in Table 1.

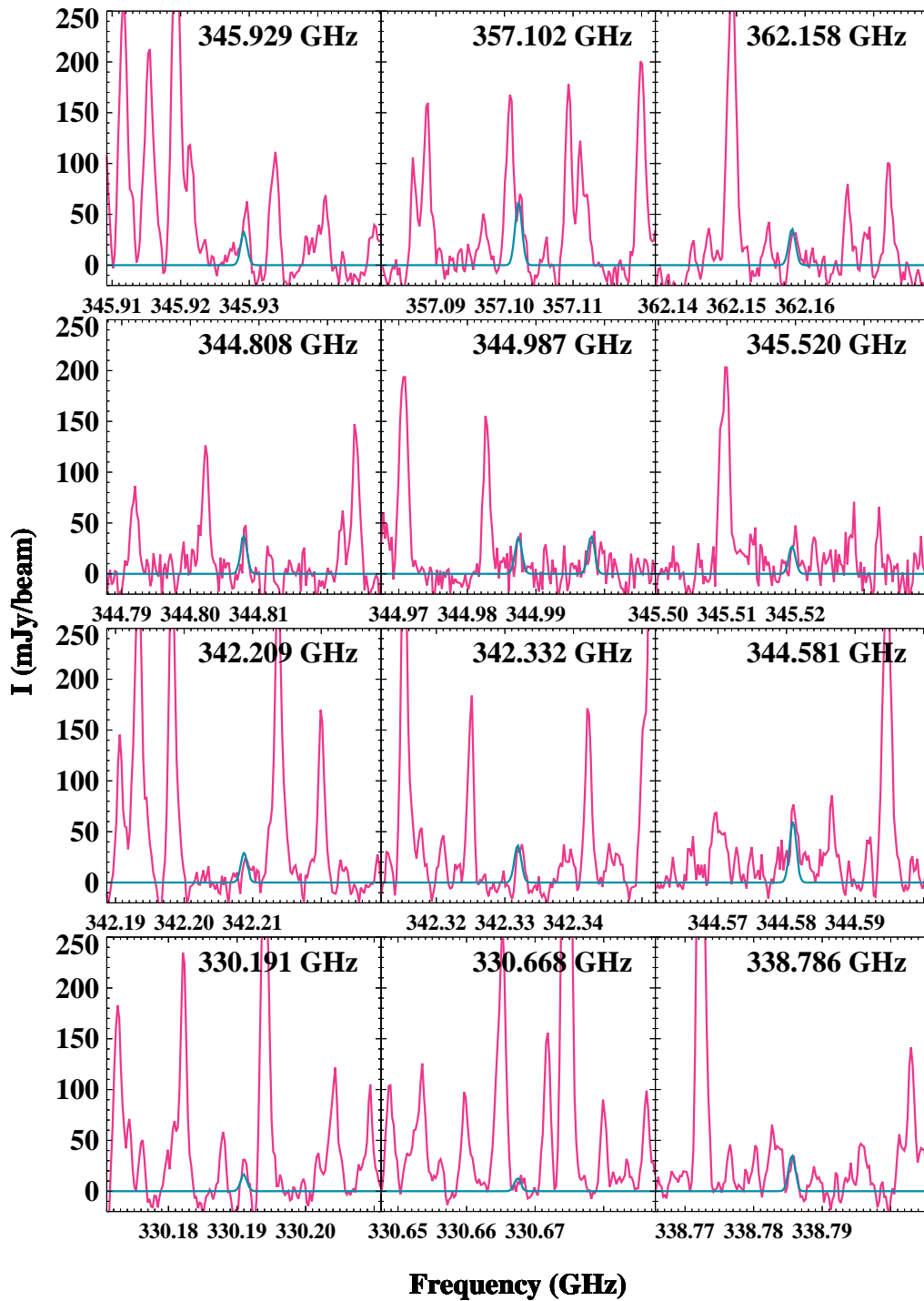


Figure B2. Twelve selected lines of $^{34}\text{SO}_2$. Idem Fig. B1.

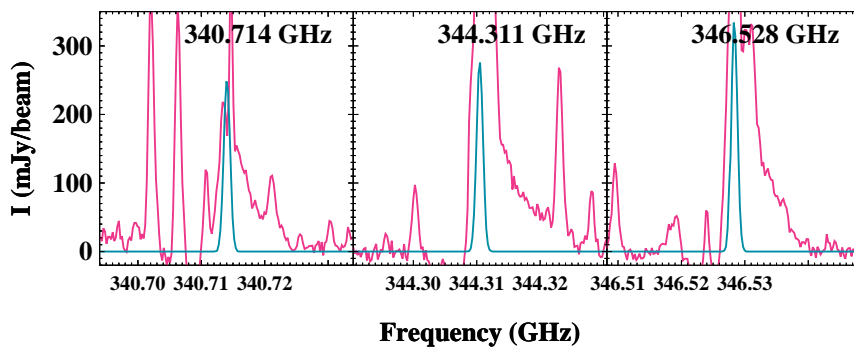


Figure B3. Three selected lines of SO in the $\nu = 0$ state. Idem Fig. B1.

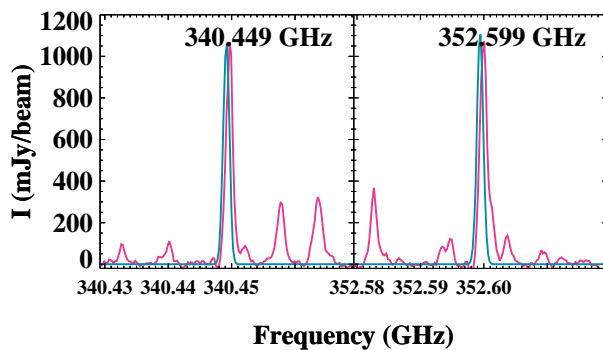


Figure B4. Two lines of OCS in the $\nu = 0$ state. Idem Fig. B1.

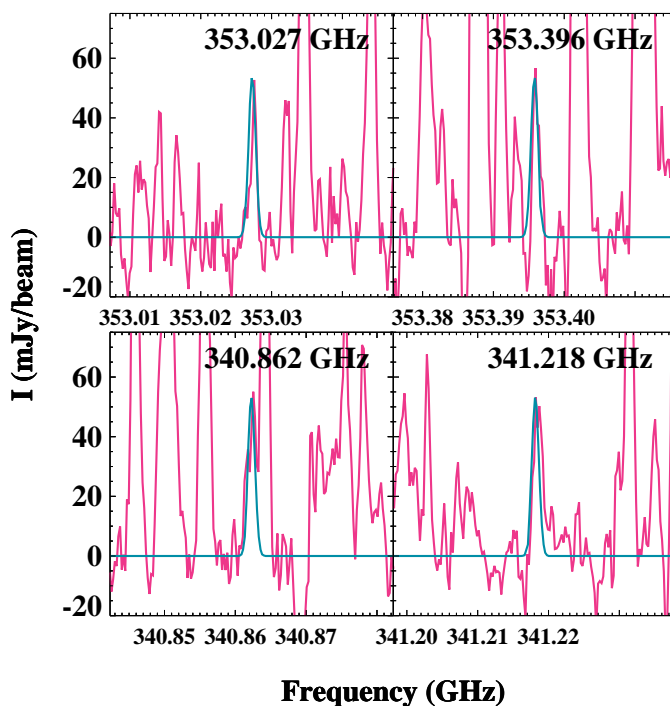


Figure B5. Four lines of OCS in the $\nu_2 = 1$ state. Idem Fig. B1.

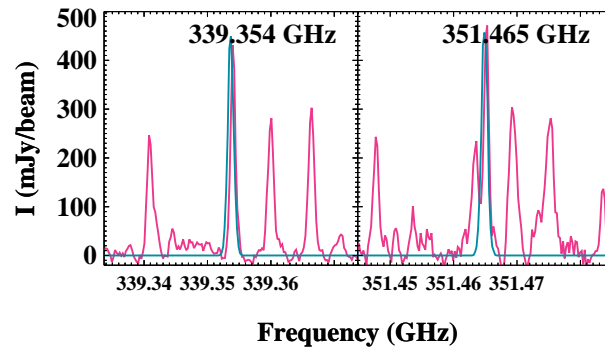


Figure B6. Two lines of O¹³CS. Idem Fig. B1.

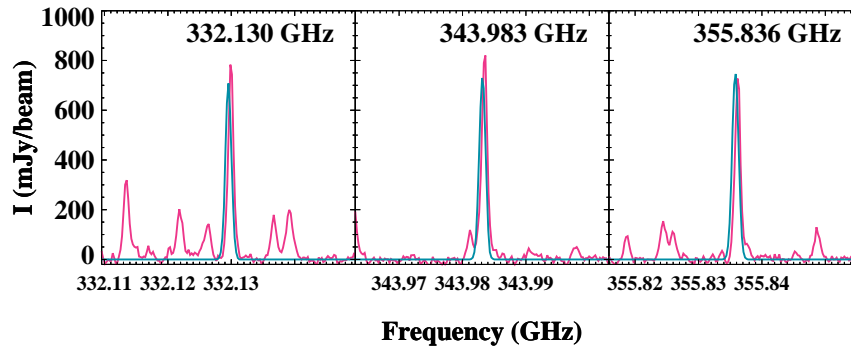


Figure B7. Three lines of OC³⁴S. Idem Fig. B1.

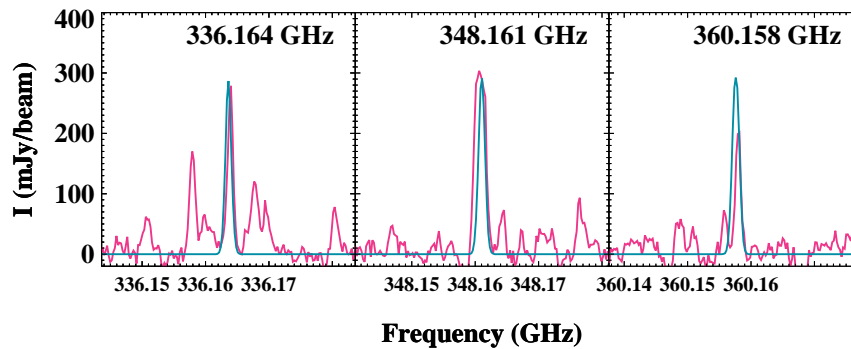


Figure B8. Three lines of OC³³S. Idem Fig. B1.

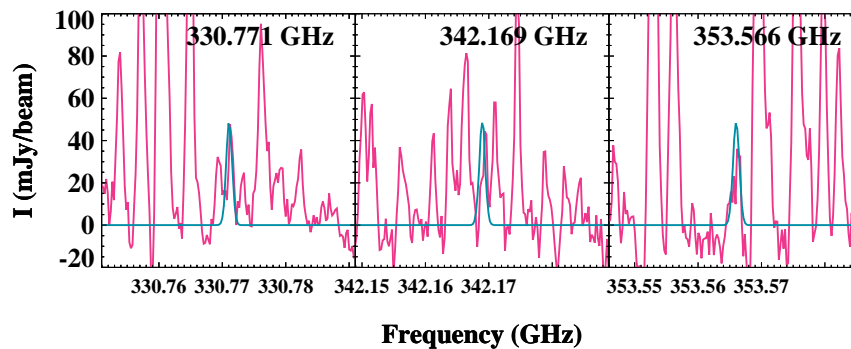


Figure B9. Three lines of ¹⁸OCS. Idem Fig. B1.

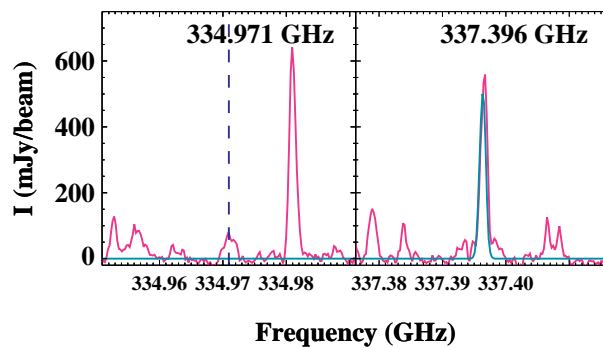


Figure B10. Two lines of $C^{34}S$ in the $\nu = 0, 1$ state. Idem Fig. B1. The vertical blue dashed line in one of the panels indicates the position of the line that is too weak to generate an emission line under the assumed conditions.

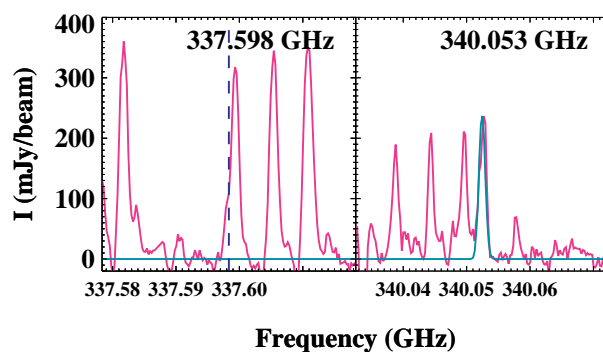


Figure B11. Two lines of $C^{33}S$ in the $\nu = 0, 1$ state. Idem Fig. B1. The vertical blue dashed line in one of the panels indicates the position of the line that is too weak to generate an emission line under the assumed conditions.

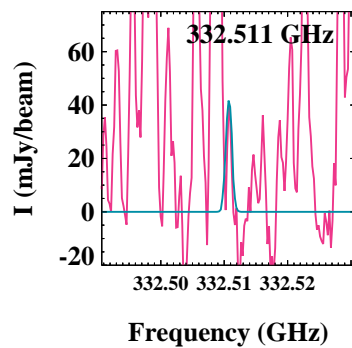


Figure B12. A line of $C^{36}S$. Idem Fig. B1.

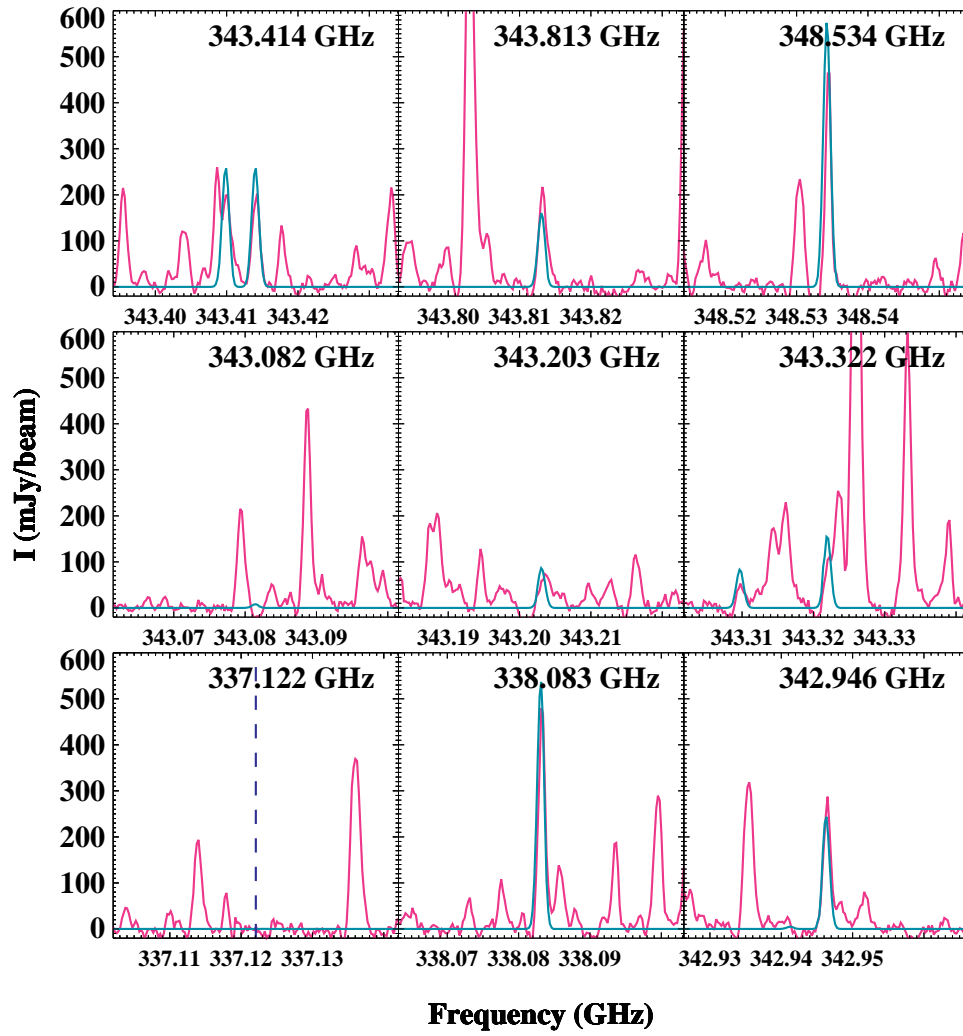


Figure B13. Nine selected lines of H₂CS. Idem Fig. B1. The vertical blue dashed line in one of the panels indicates the position of the line that is too weak to generate an emission line under the assumed conditions.

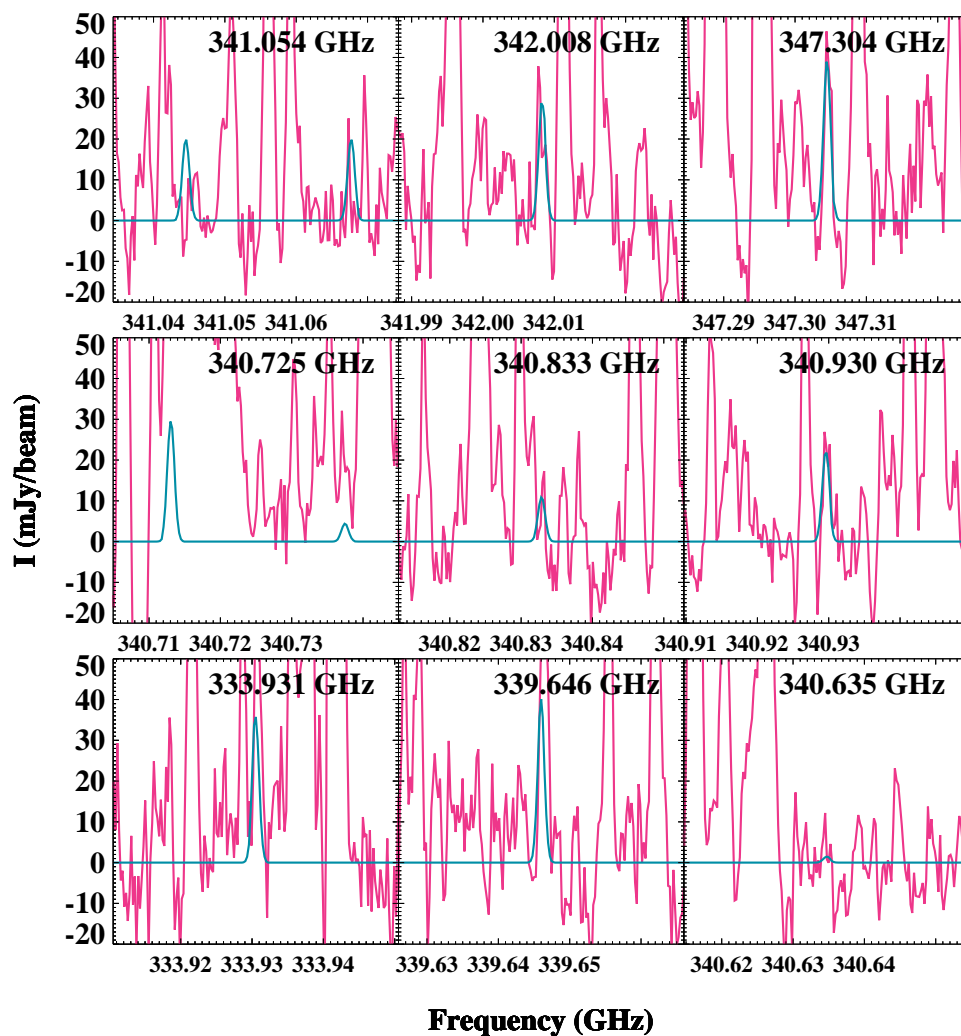


Figure B14. Nine selected lines of HDCS. Idem Fig. B1.

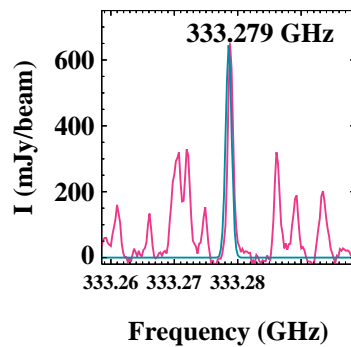


Figure B15. A selected line of HDS. Idem Fig. B1.

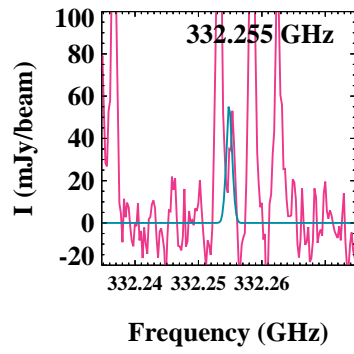


Figure B16. A selected line of HD³⁴S. Idem Fig. B1.

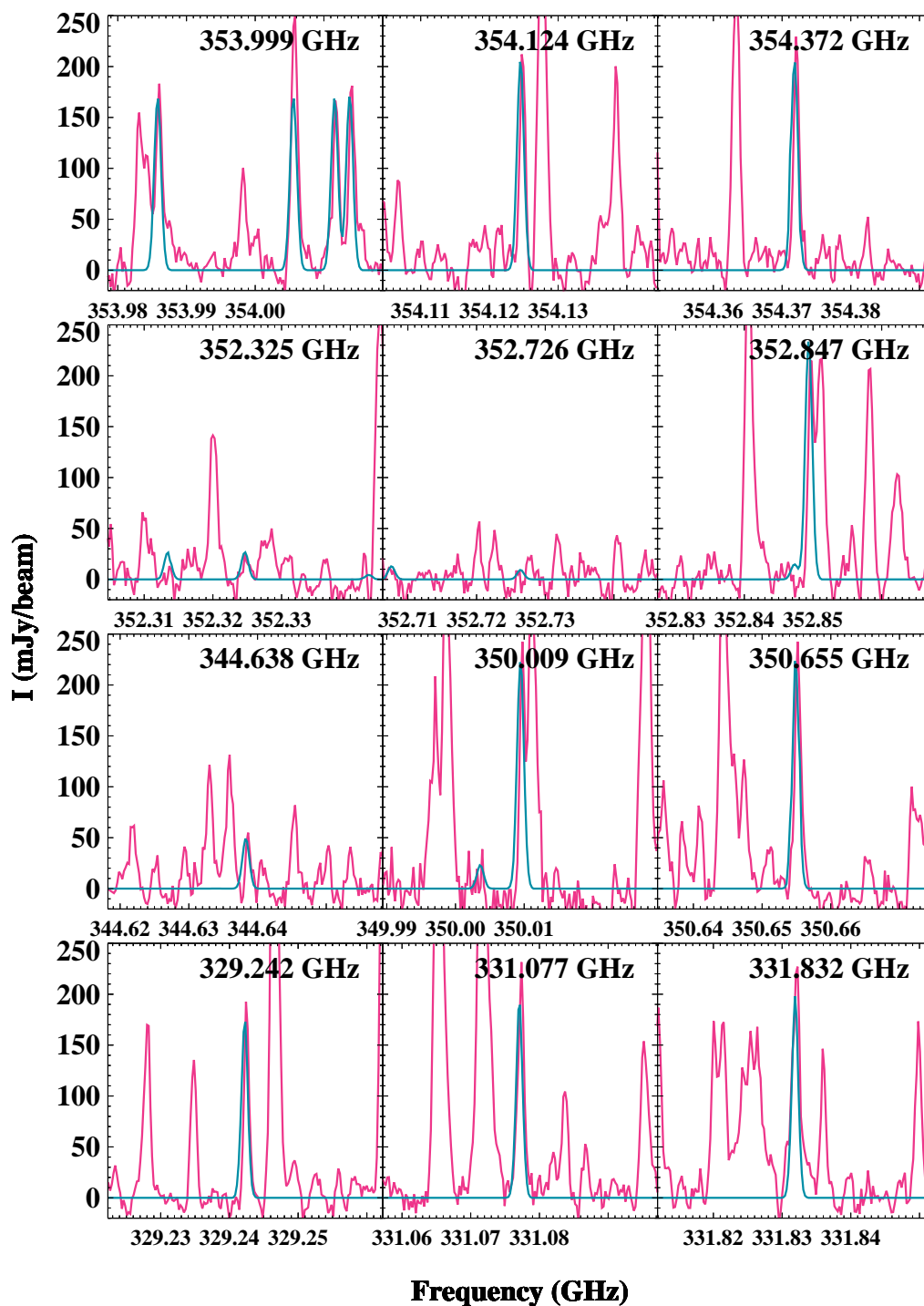


Figure B17. Twelve selected lines of CH_3SH in the $\nu = 0 - 2$ state. Idem Fig. B1.

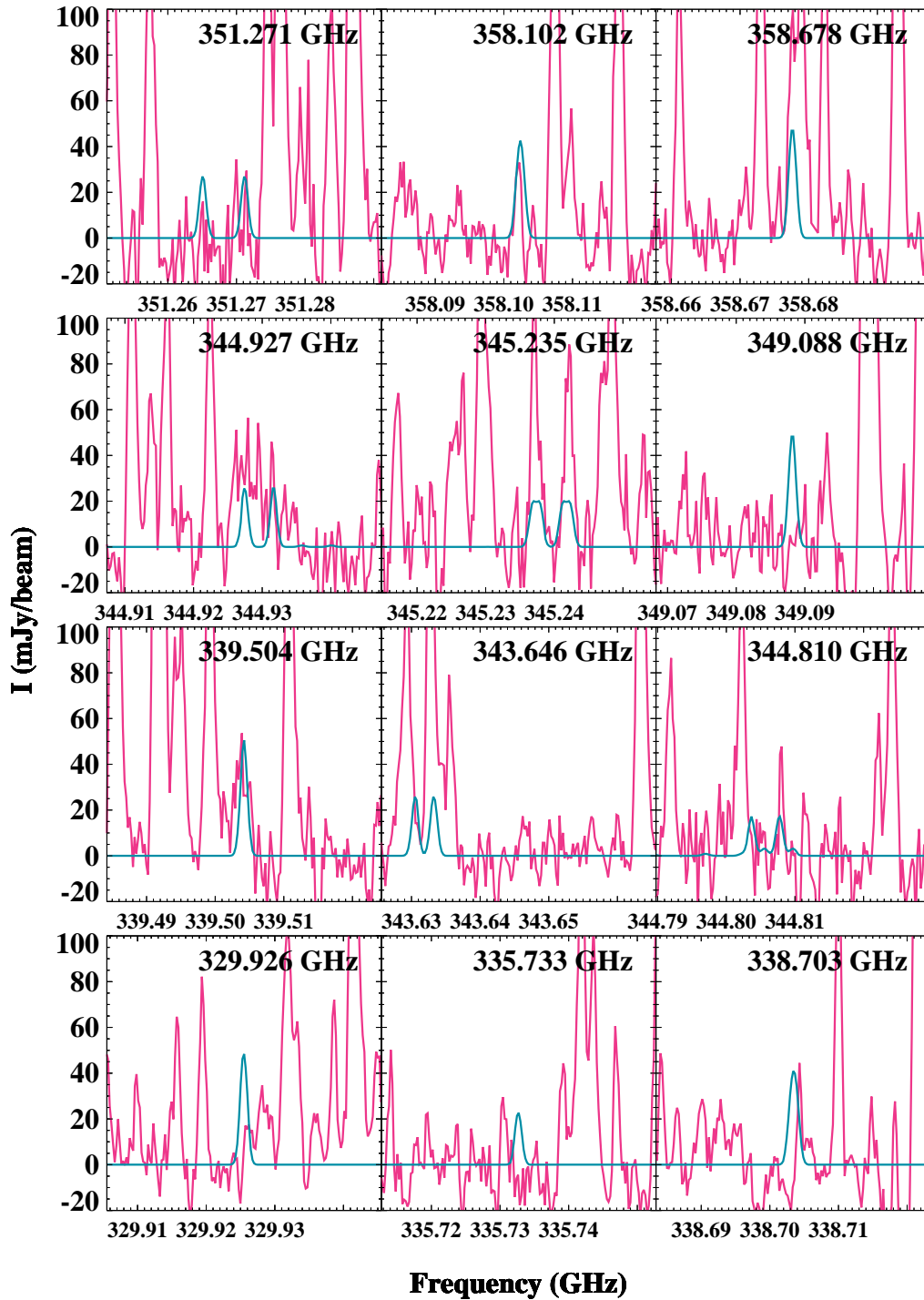


Figure B18. Twelve selected lines of gauche-C₂H₅SH. Idem Fig. B1.

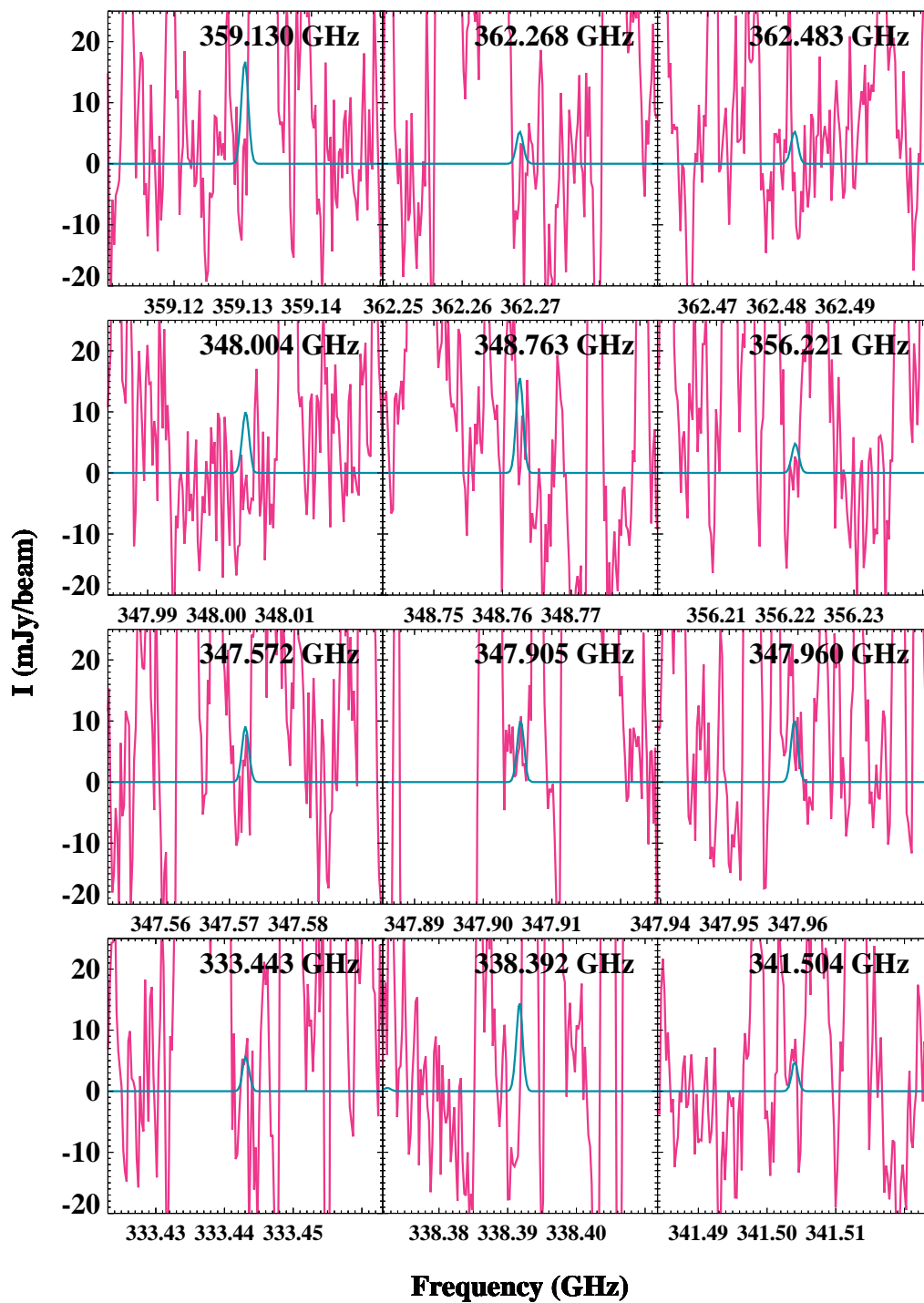


Figure B19. Twelve selected lines of anti-C₂H₅SH. Idem Fig. B1.

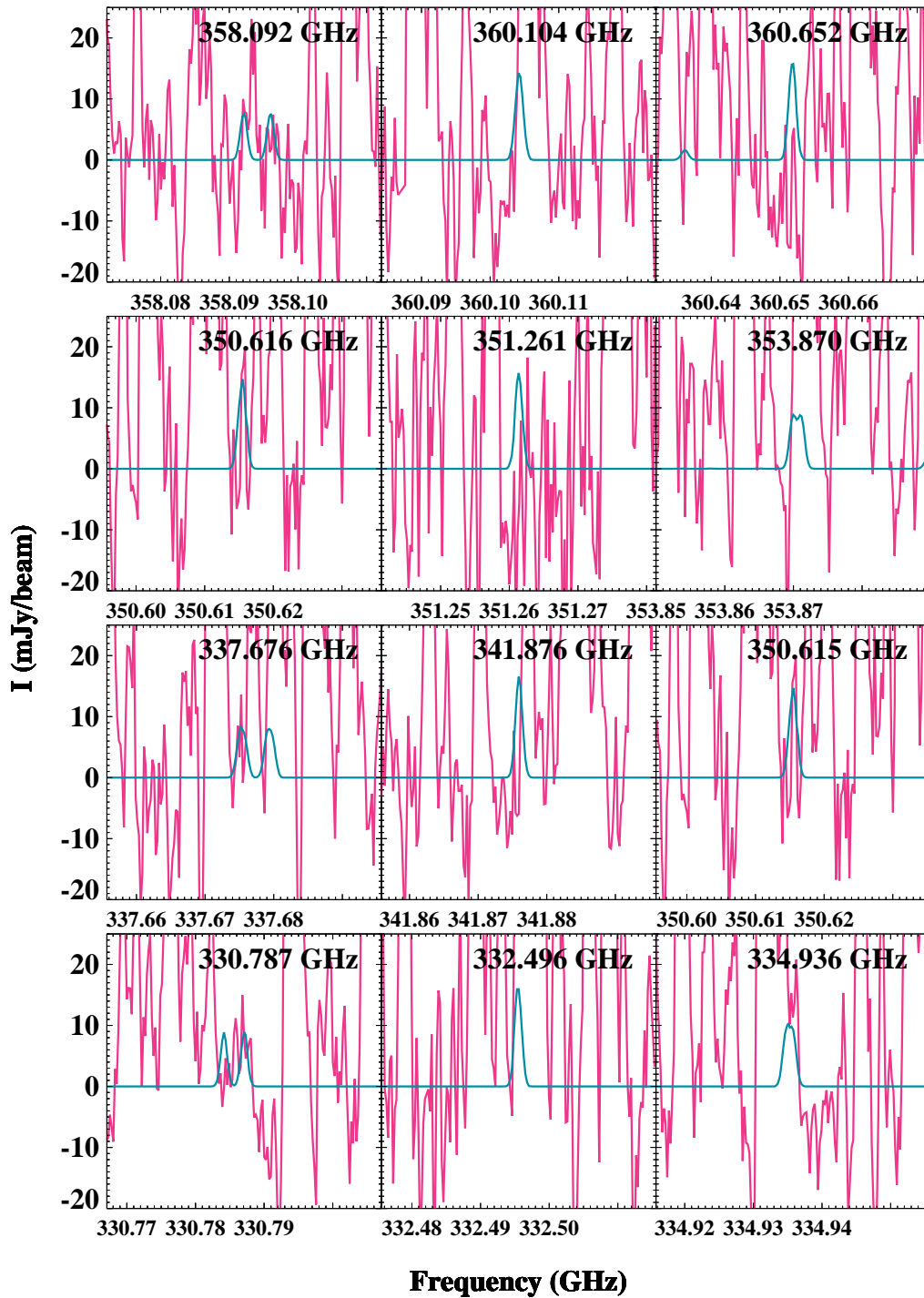


Figure B20. Twelve selected lines of gauche-C₂H₅³⁴SH. Idem Fig. B1.

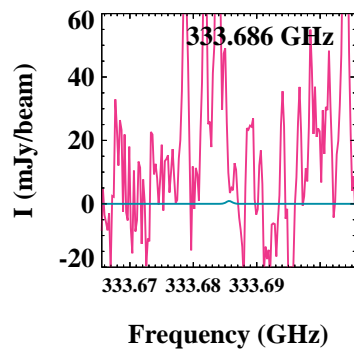


Figure B21. A line of S_2 . Idem Fig. B1.

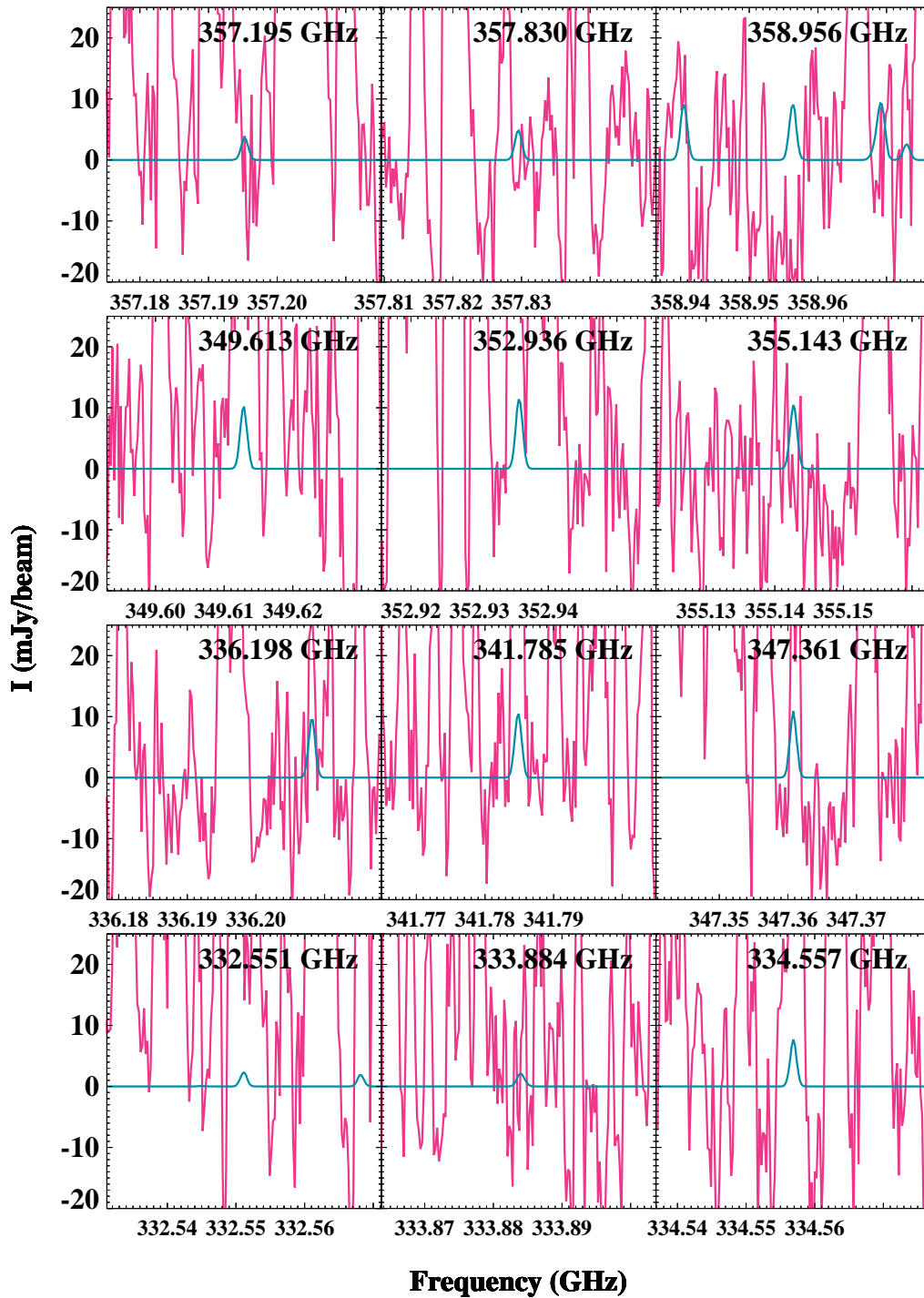


Figure B22. Twelve selected lines of S_3 . Idem Fig. B1.

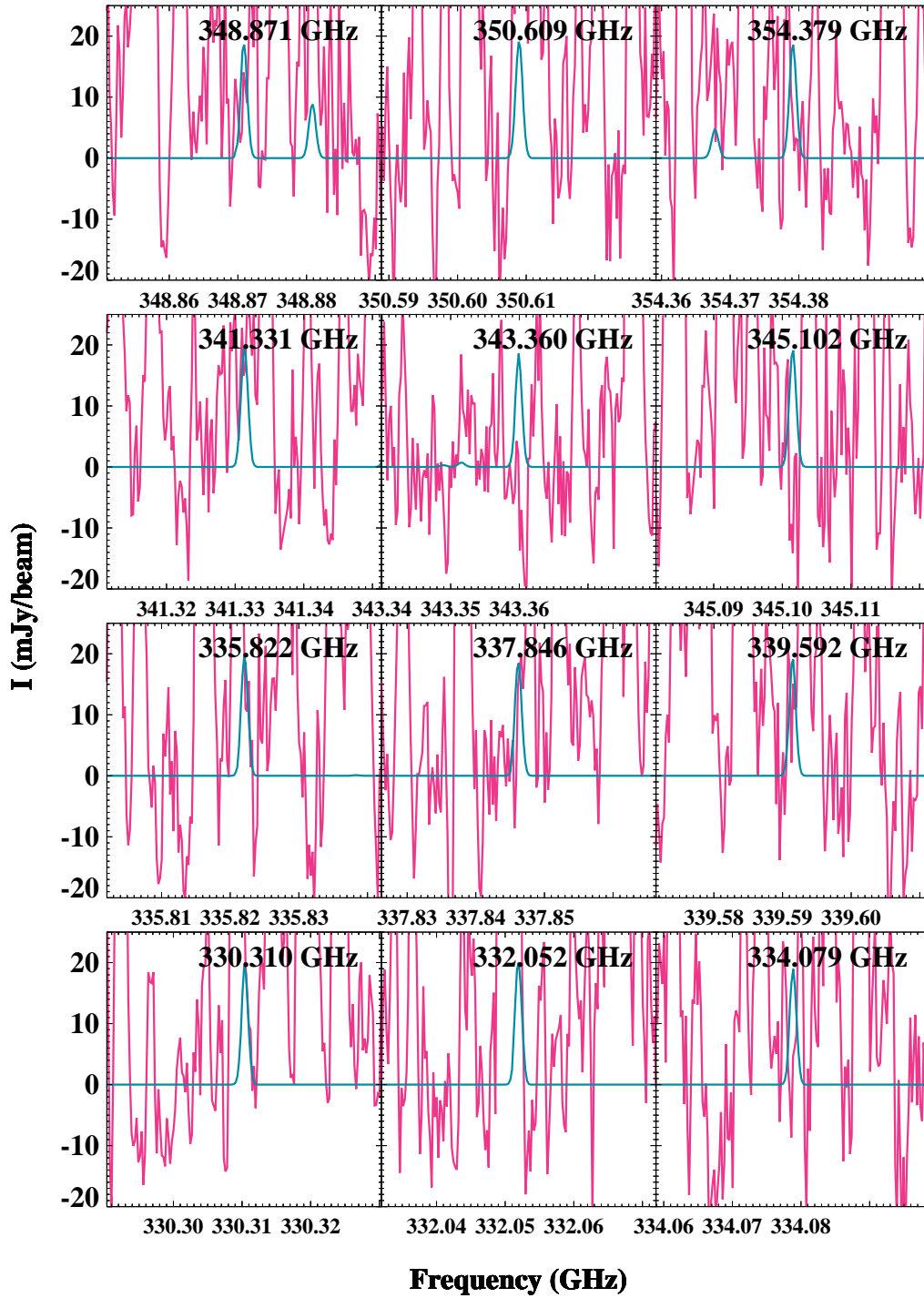


Figure B23. Twelve selected lines of S_4 . Idem Fig. B1.

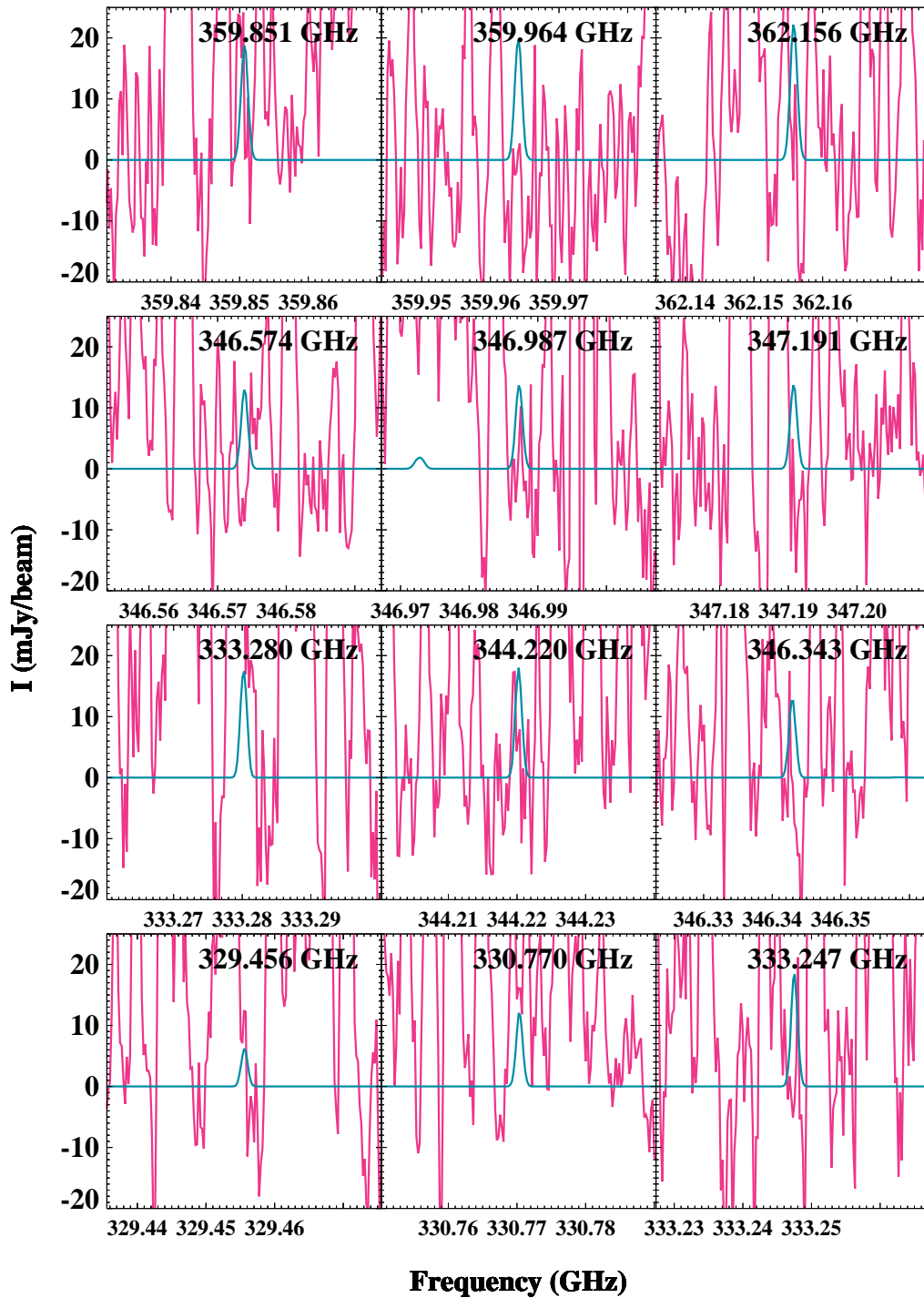


Figure B24. Twelve selected lines of HS₂. Idem Fig. B1.

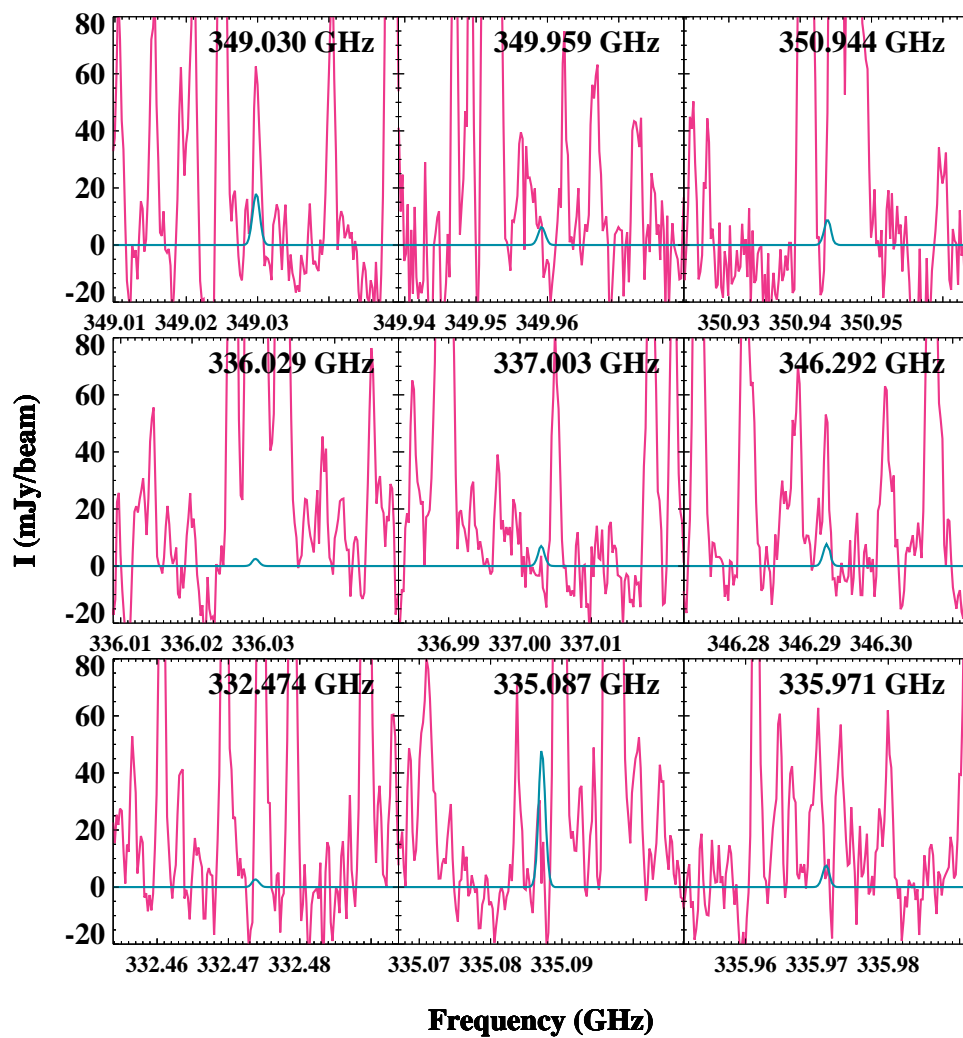


Figure B25. Nine selected lines of H_2S_2 . Idem Fig. B1.

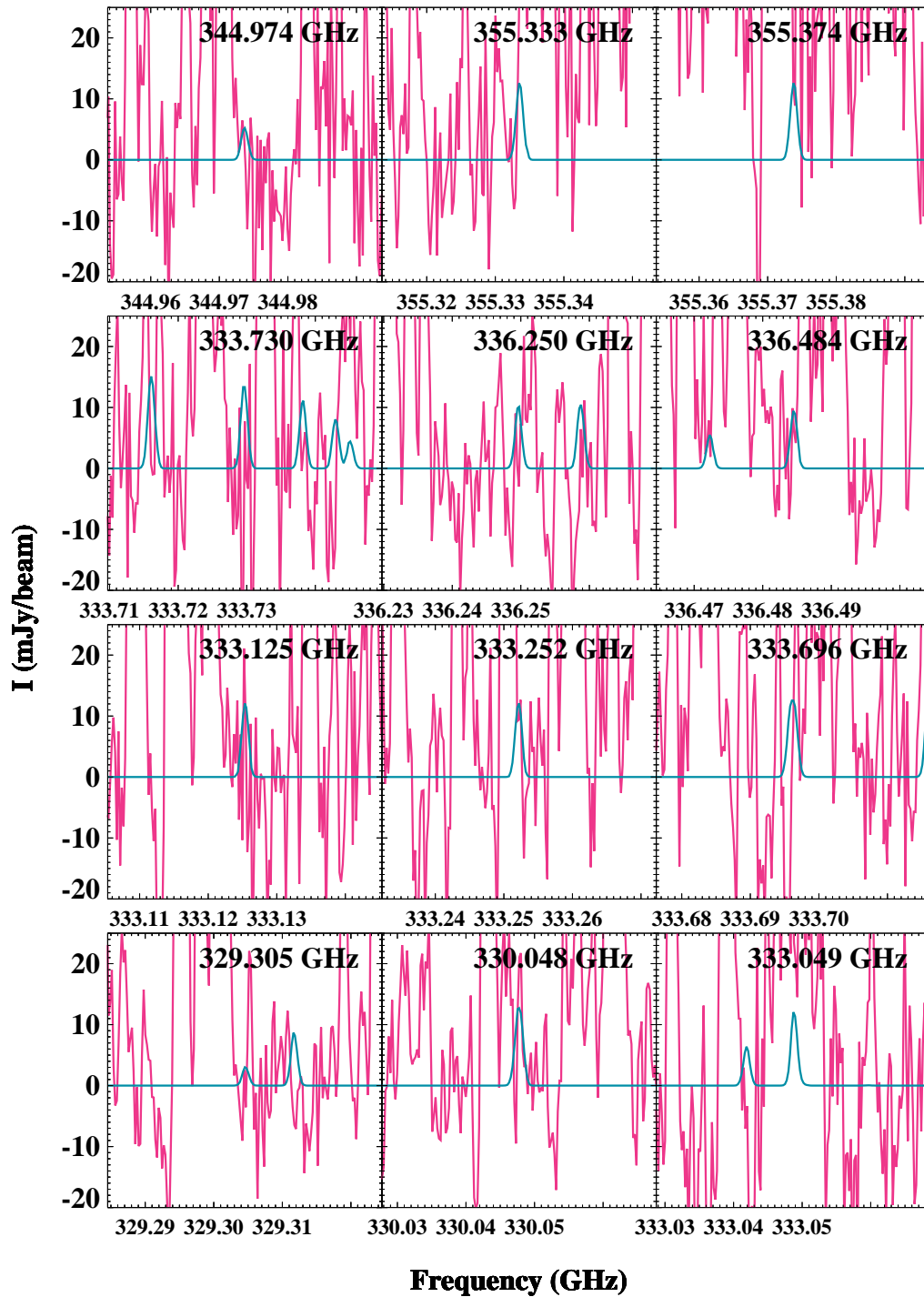


Figure B26. Twelve selected lines of S₂O in the $\nu = 0$ state. Idem Fig. B1.

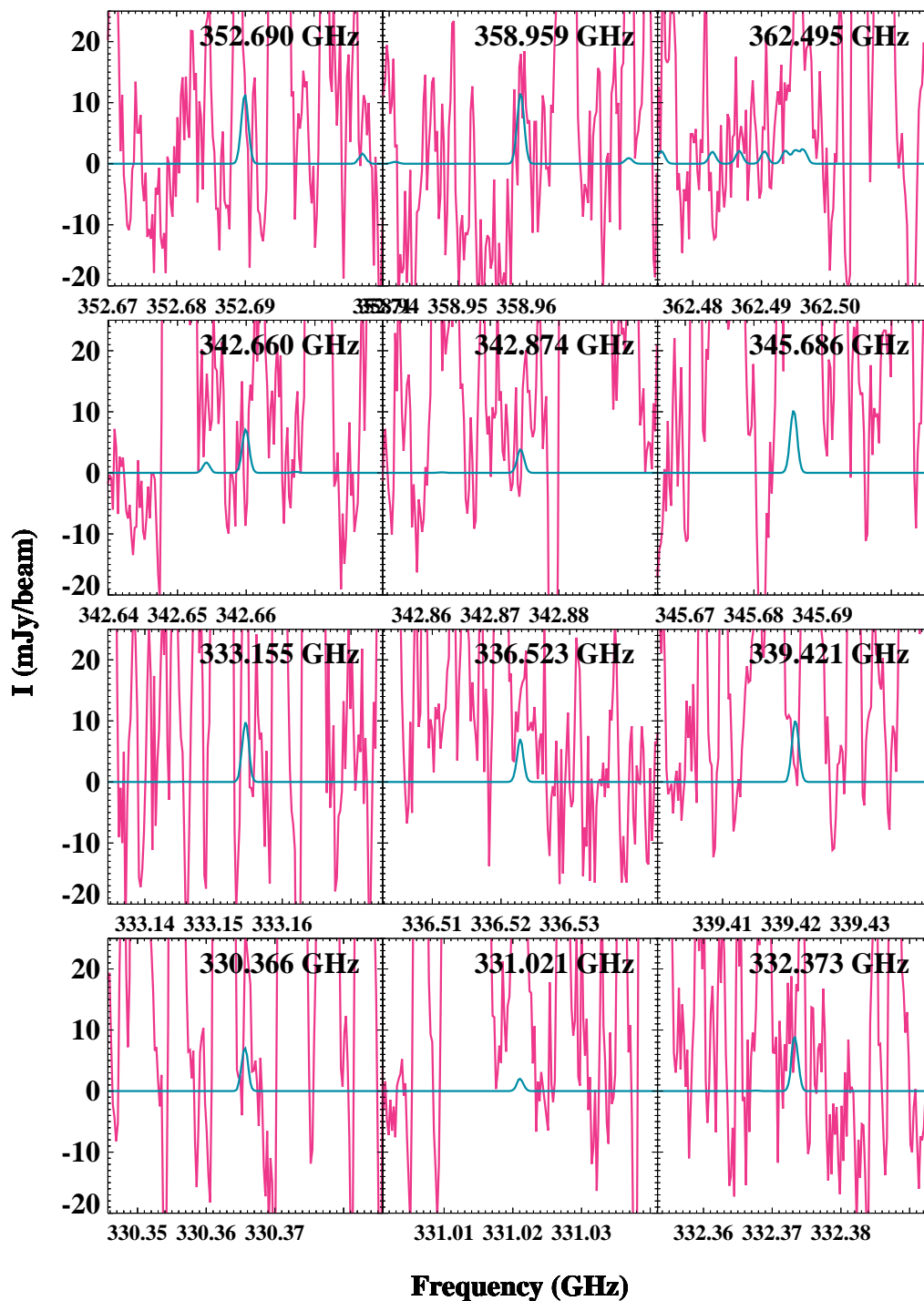


Figure B27. Twelve selected lines of *cis*-S₂O₂. Idem Fig. B1.

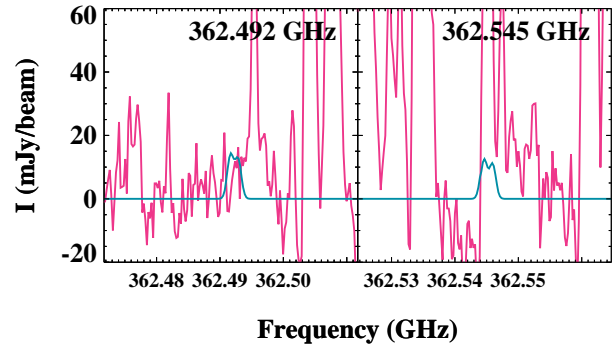


Figure B28. Two selected lines of HCS. Idem Fig. B1.

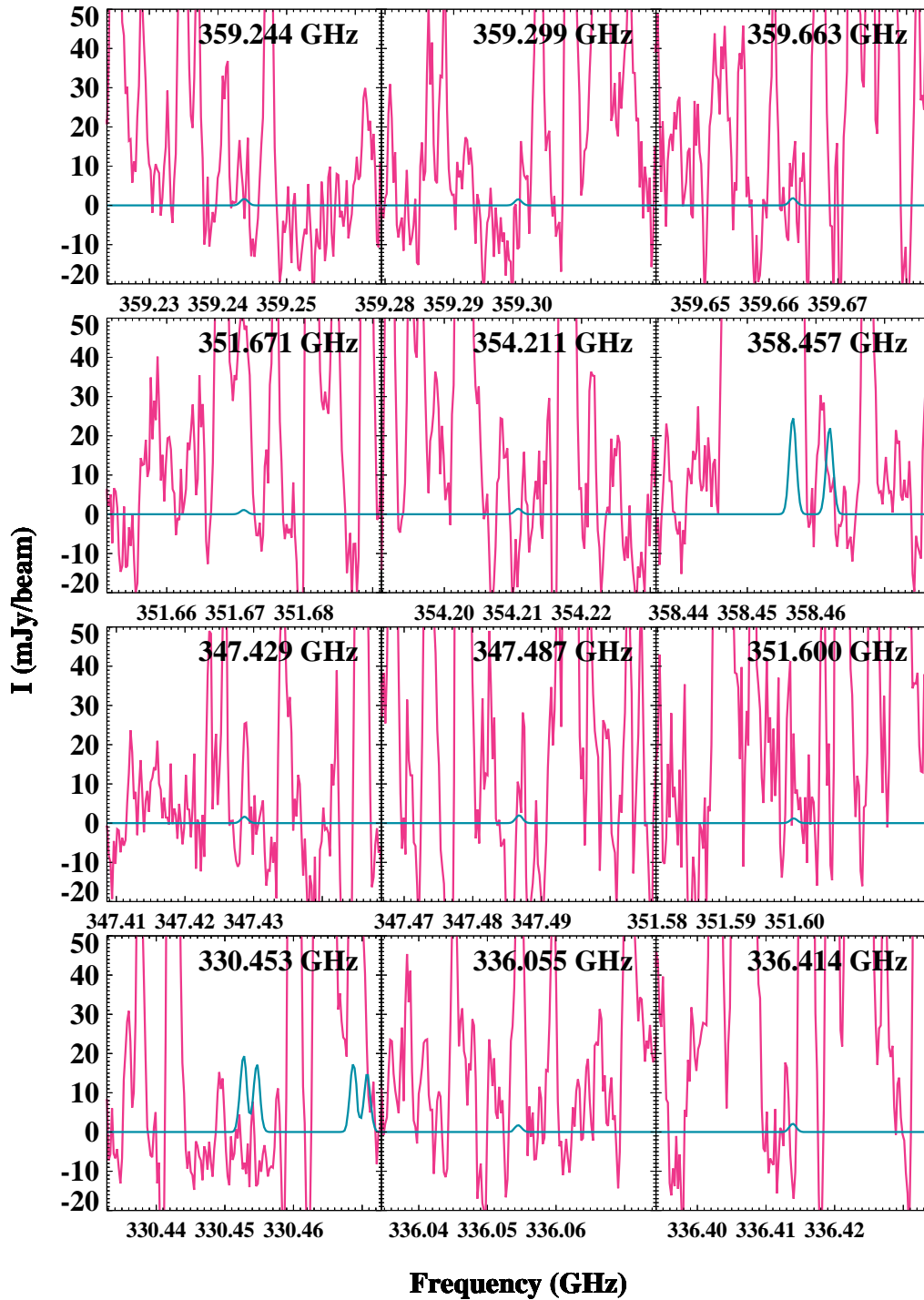


Figure B29. Twelve selected lines of HSC. Idem Fig. B1.

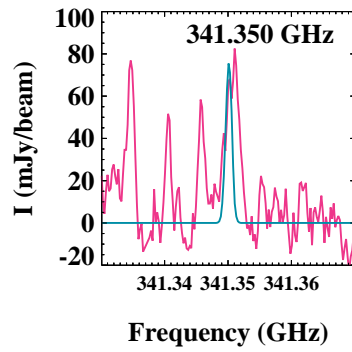


Figure B30. A line of HCS⁺. Idem Fig. B1.

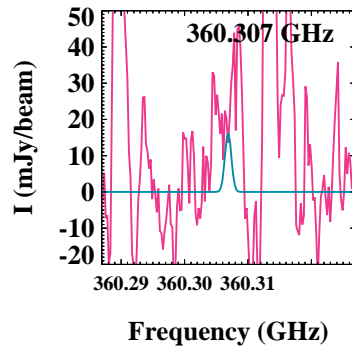


Figure B31. A line of DCS⁺. Idem Fig. B1.

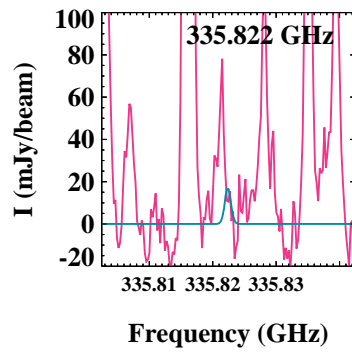


Figure B32. A line of HC³⁴S⁺. Idem Fig. B1.

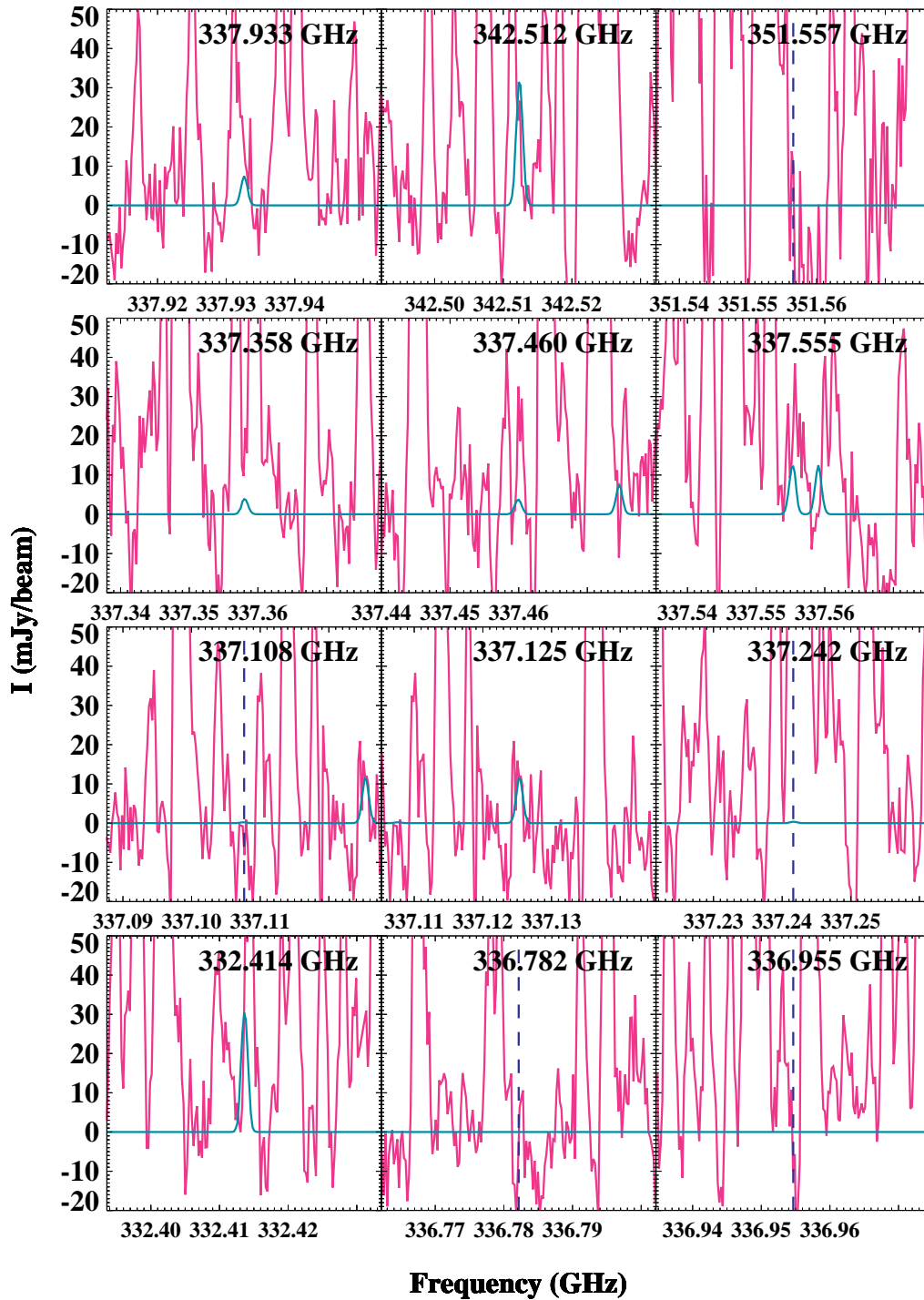


Figure B33. Fourteen selected lines of $\text{H}_2\text{C}^{34}\text{S}$. Idem Fig. B1. The vertical blue dashed line in one of the panels indicates the position of the line that is too weak to generate an emission line under the assumed conditions.

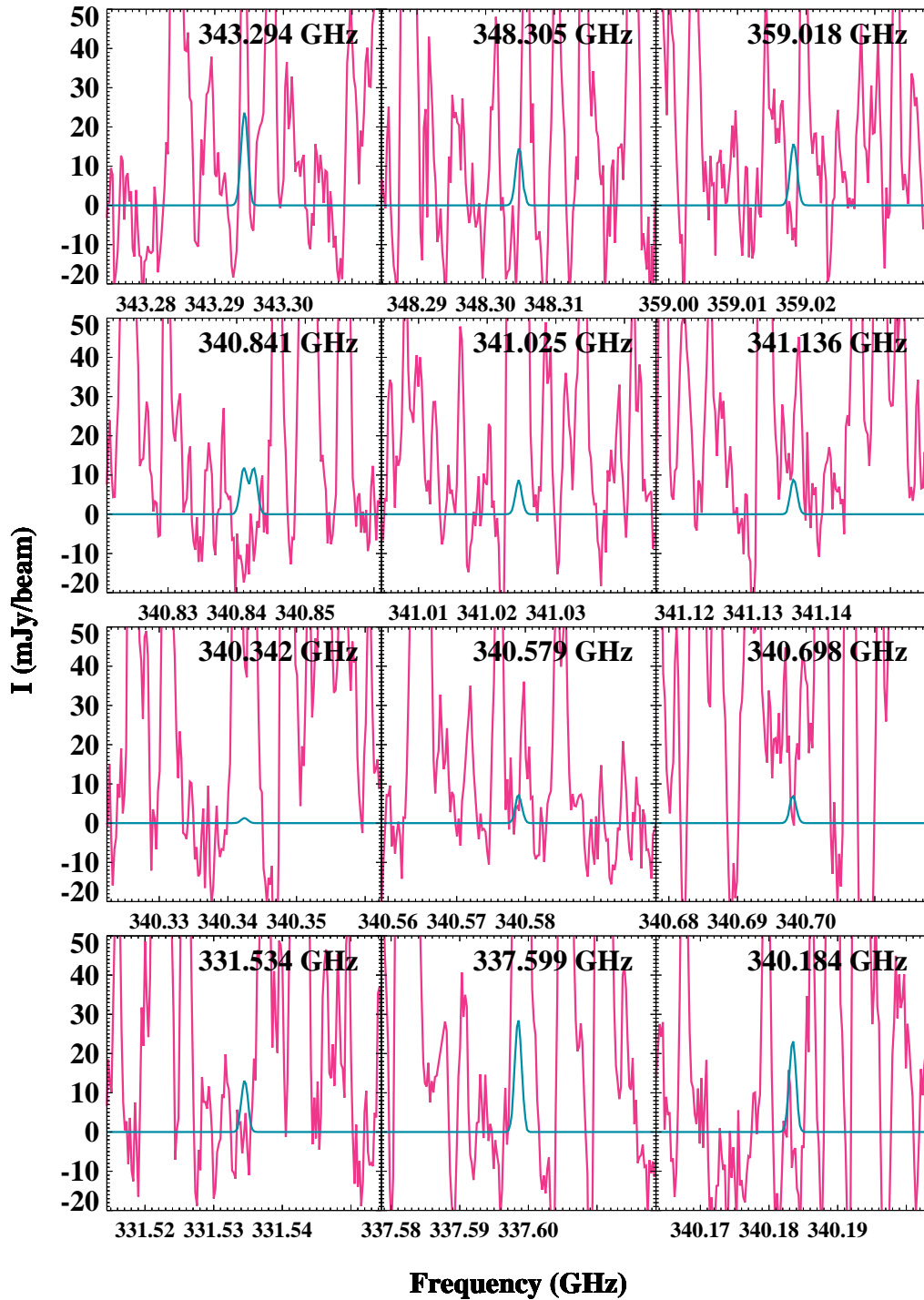


Figure B34. Twelve selected lines of D_2CS . Idem Fig. B1.

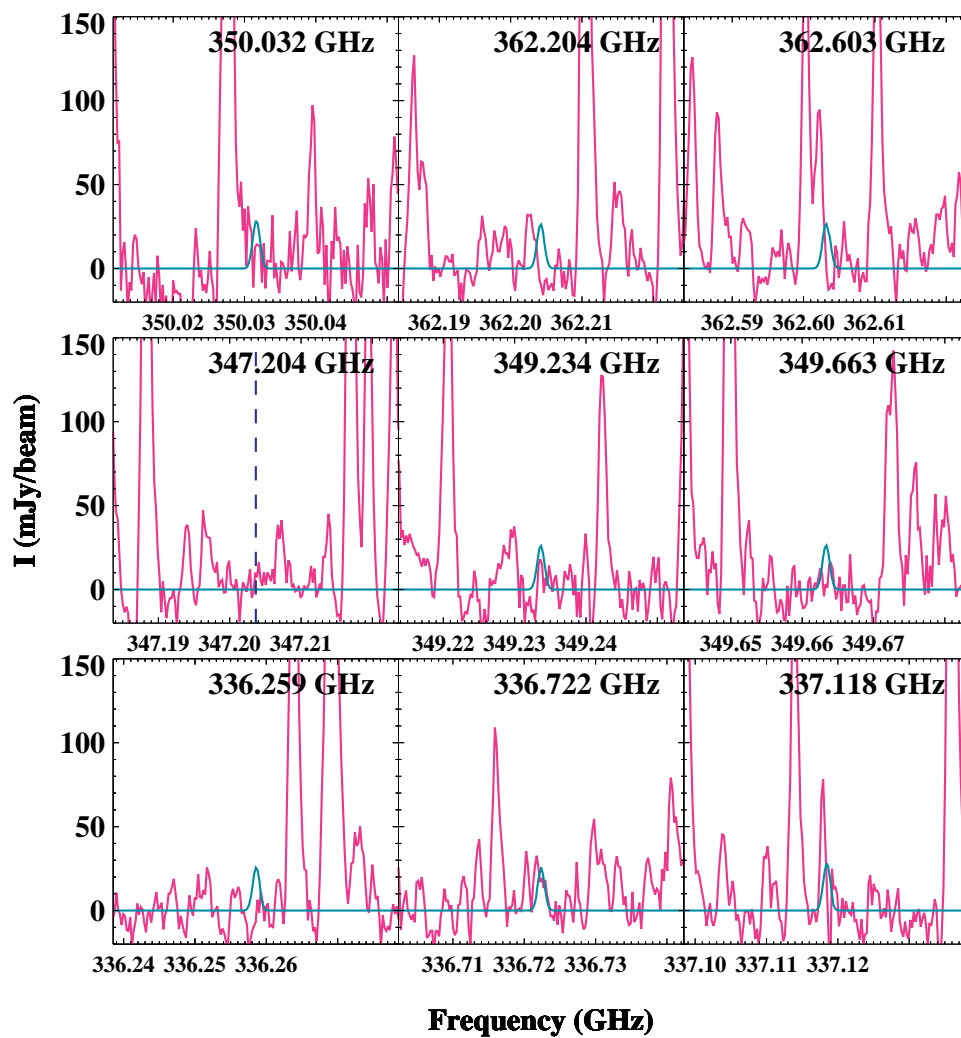


Figure B35. Nine selected lines of CCS. Idem Fig. B1. The vertical blue dashed line in one of the panels indicates the position of the line that is too weak to generate an emission line under the assumed conditions.

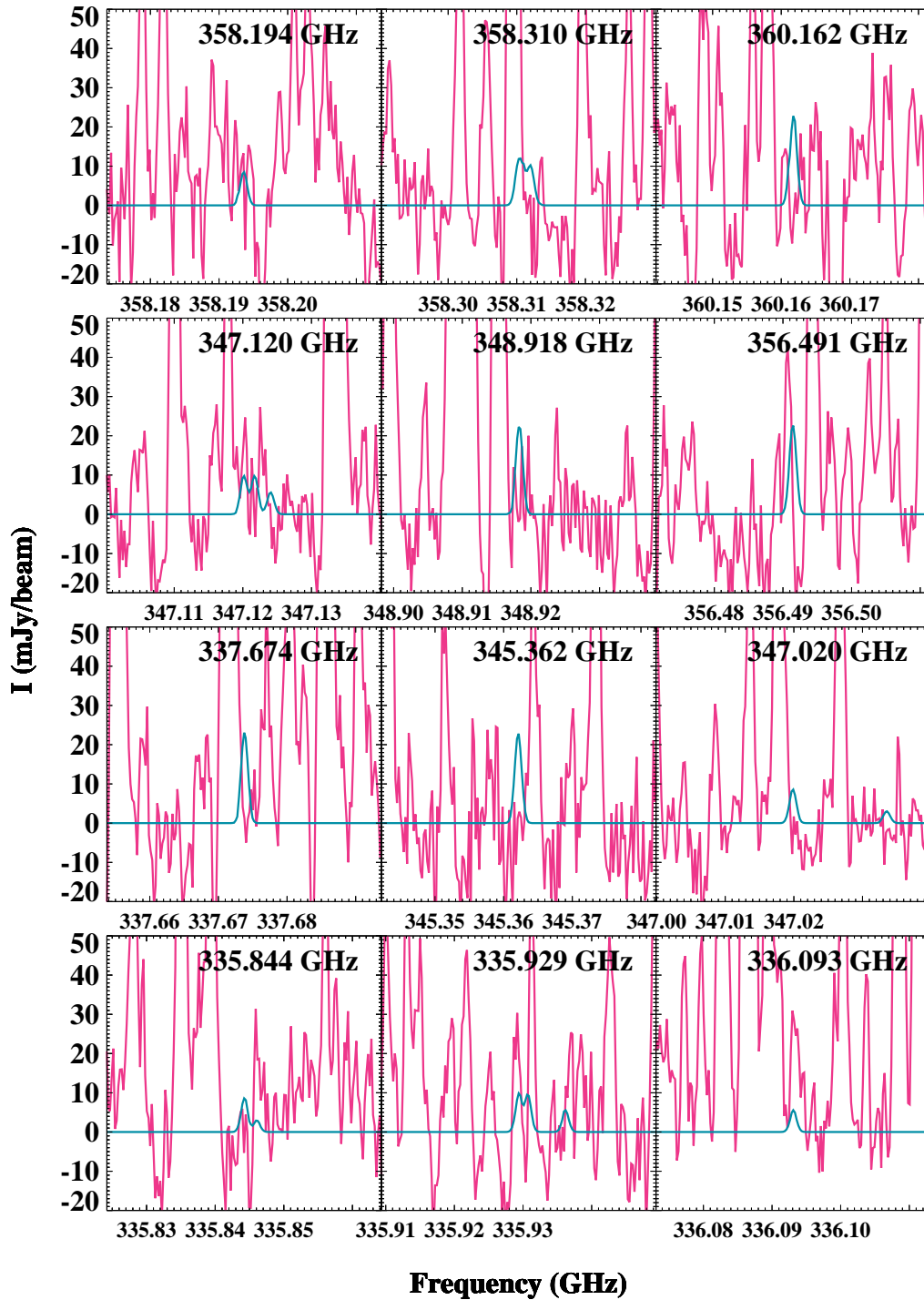


Figure B36. Twelve selected lines of $\text{H}_2\text{C}_2\text{S}$. Idem Fig. B1.

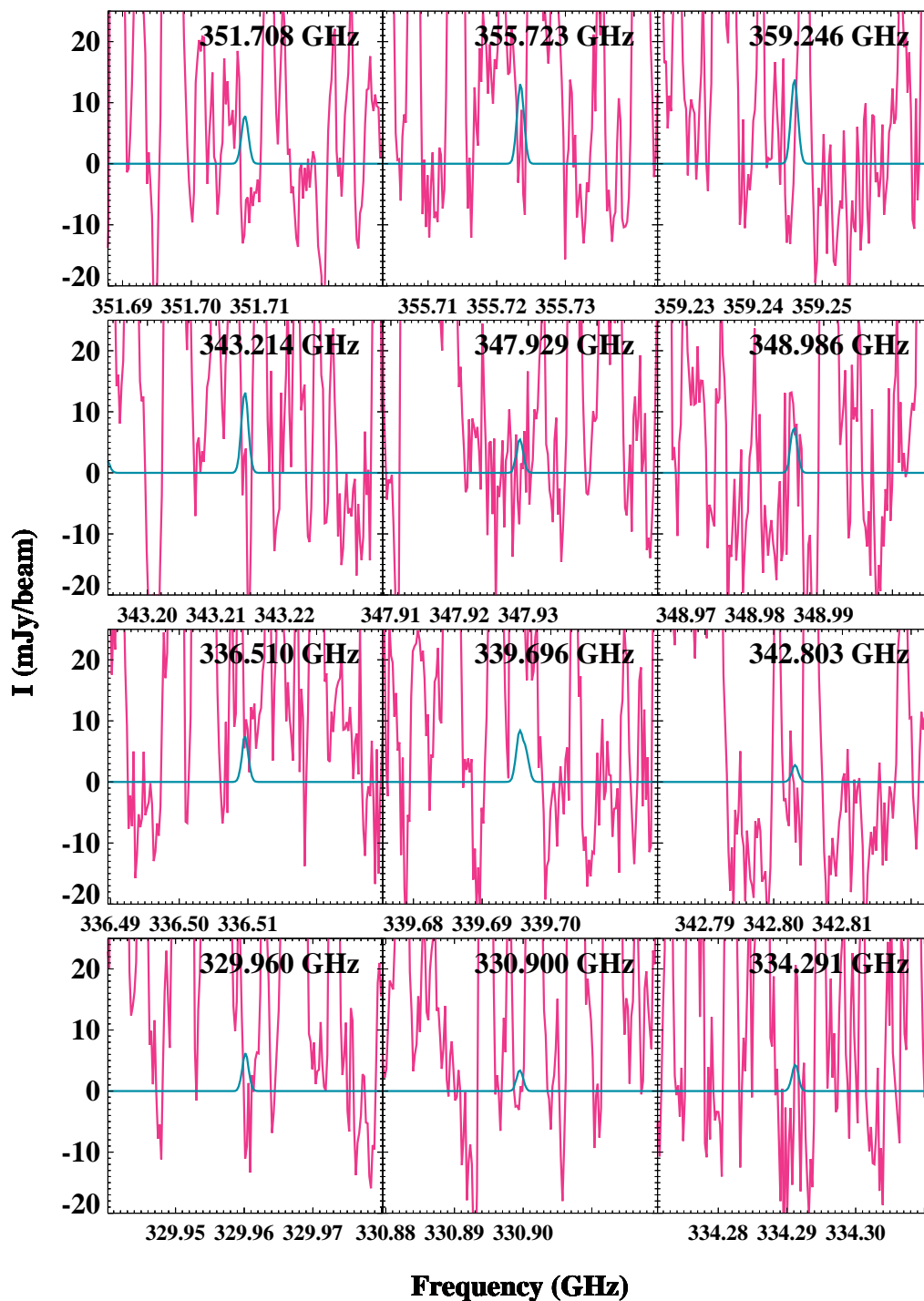


Figure B37. Twelve selected lines of $c\text{-C}_2\text{H}_4\text{S}$. Idem Fig. B1.

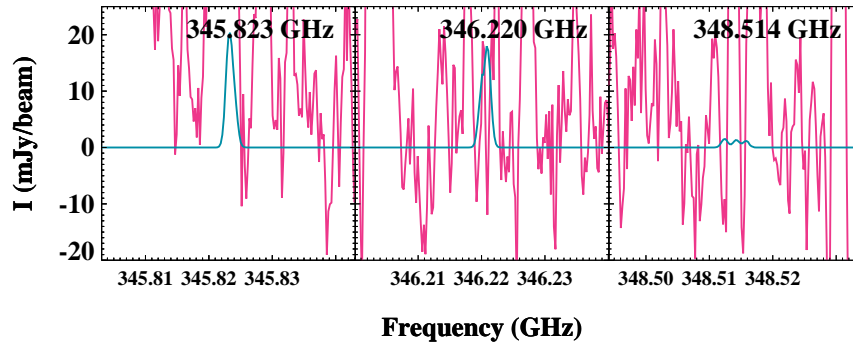


Figure B38. Three selected lines of NS in the $v = 0$ state. Idem Fig. B1.

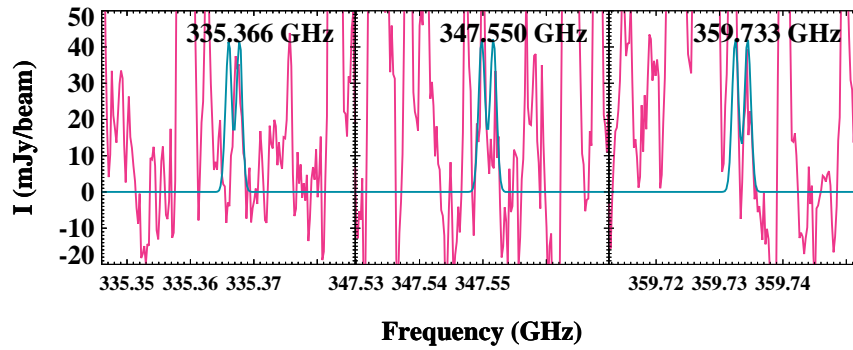


Figure B39. Three lines of NCS. Idem Fig. B1.

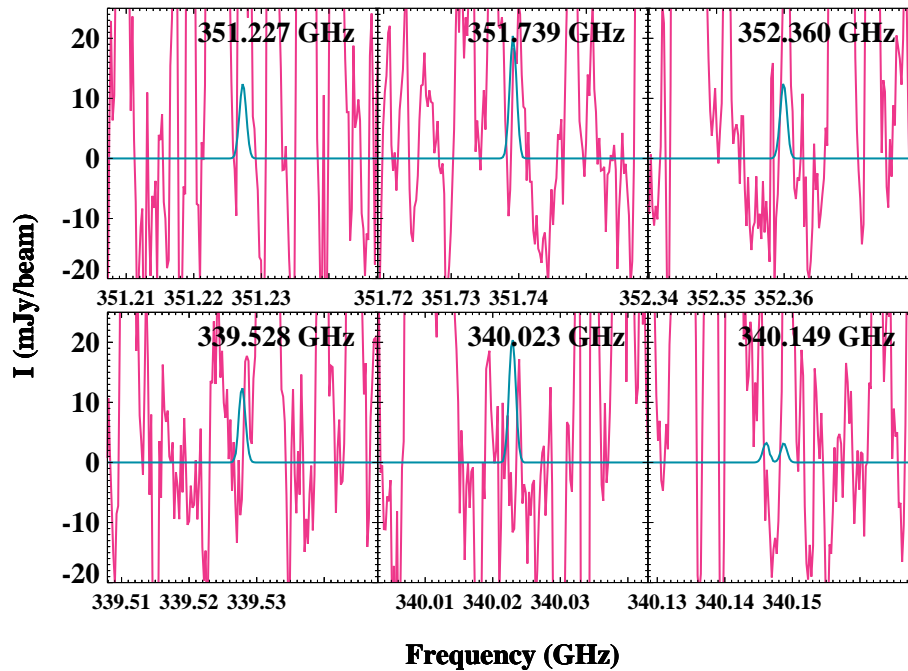


Figure B40. Nine lines of HNCS of the a-type. Idem Fig. B1.

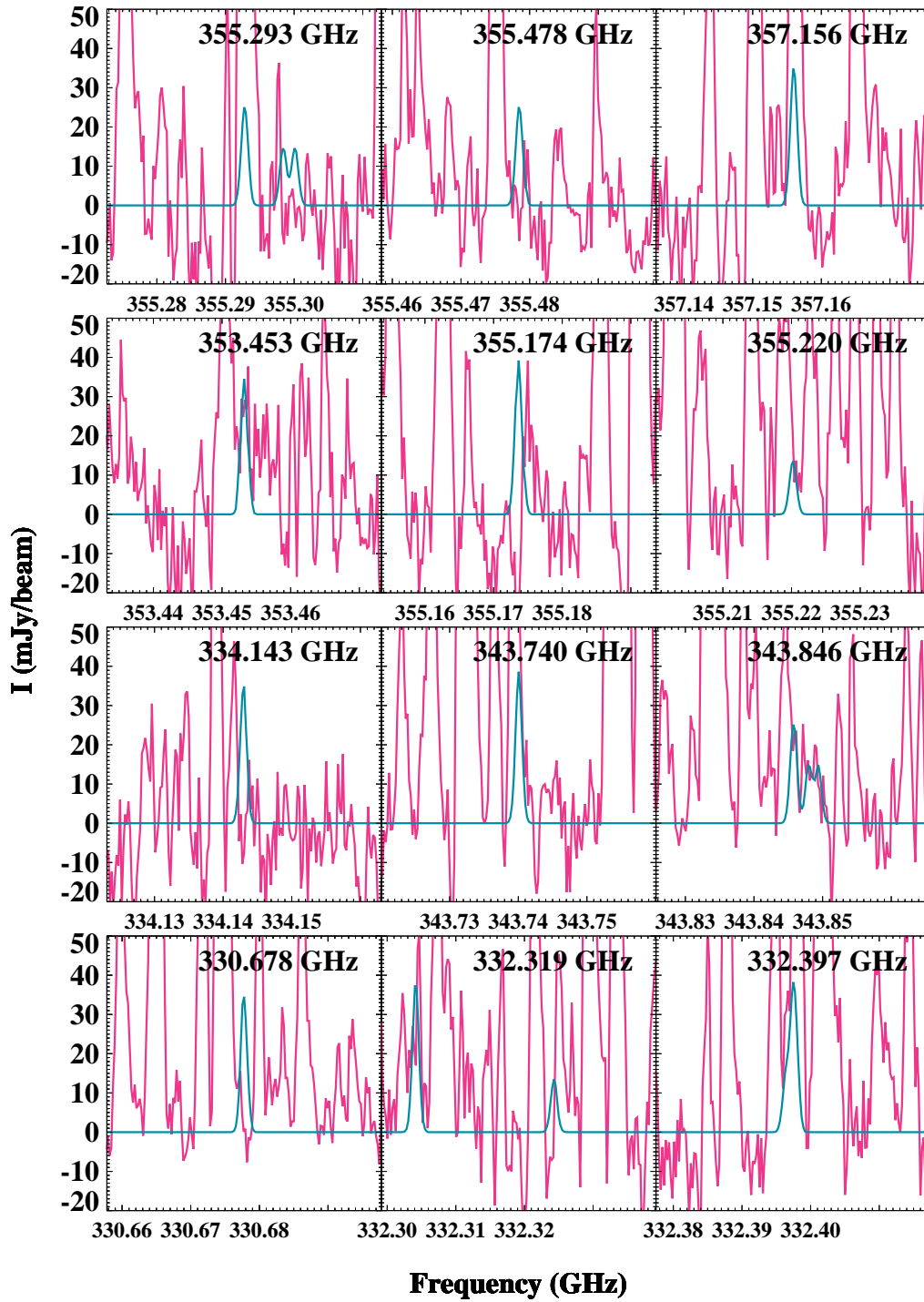


Figure B41. Twelve selected lines of HSCN. Idem Fig. B1.

APPENDIX C: SPECTROSCOPIC LABORATORY INFORMATION

moments for all detected or possibly detected species are given below. Furthermore, the references with laboratory measurements in the range of the PILS survey in cases, in which the primary reference does not cover such data or if these data are an important contribution to the line list, are also included.

C1 SO₂

The $\nu = 0$ and $\nu_2 = 1$ entries for the main isotopic species are based on Müller & Brünken (2005), those for ³⁴SO₂ – on Belov et al. (1998). The dipole moment of SO₂ in several vibrational states was determined by Patel, Margolese & Dyke (1979).

C2 SO

The SO entry is based on Bogey et al. (1997). Its dipole moment was measured by Powell & Lide (1964).

C3 OCS

The main sources for the OCS entries are: Golubiatnikov et al. (2005) for OCS, $\nu = 0$; Morino, Yamada & Maki (2000) for OCS, $\nu_2 = 1$; Dubrulle et al. (1980) for O¹³CS, OC³⁴S and OC³³S. Dipole moment values were determined for OCS in various vibrational states and for several isotopic species by Tanaka, Tanaka & Suzuki (1985).

C4 CS

The CS entries are based on Müller et al. (2005), and the main sources of laboratory data are Bogey, Demuyneck & Destombes (1982) and Ahrens & Winnewisser (1999). The dipole moments of CS in $\nu = 0$ and 1 were measured by Winnewisser & Cook (1968).

C5 H₂CS

The H₂CS data are largely from Maeda et al. (2008), those of HDCS are from Minowa et al. (1997). Fabricant, Krieger & Muentner (1977) determined the dipole moment of H₂CS.

C6 H₂S

The H₂S entry is based to a considerable extent on Belov et al. (1995). The entries of HDS and HD³⁴S are based on Camy-Peyret et al. (1985). The HDS transition frequencies with microwave accuracy were summarized by Helminger, Cook & De Lucia (1971). Hillger & Strandberg (1951) reported a small number of HD³⁴S and HDS transition frequencies. Viswanathan & Dyke (1984) determined dipole moments of H₂S, HDS and D₂S.

C7 CH₃SH

The CH₃SH entry is based on Xu et al. (2012) with transition frequencies in the range of our survey from Bettens et al. (1999). The information on the dipole moment components was provided by Tsunekawa et al. (1989).

The database sources, CDMS or JPL catalogues with their entry numbers, have been provided in the main text for all the species that have been searched for. In addition, the primary references on which these entries are based along with references for the dipole

APPENDIX D: ALL THE NON-DETECTED SPECIES

The one beam offset position of the PILS Band 7 dataset was searched for all the sulphur-bearing molecules available in the CDMS catalogue. All those detected are given in Table 1. All those not detected, but with a derived upper limit are given in Table 2. The following is a list of all other non-detected species at the 1σ level ($\sigma = 10$ mJy beam⁻¹ channel⁻¹ or 5 mJy beam⁻¹ km s⁻¹) and their corresponding CDMS entries in brackets: SO₂ $v_2 = 1$ (64503), ³³SO₂ (65501), S¹⁸OO (66502), S¹⁷OO (65502), SO $v = 1$ (48502), ³⁴SO (50501), ³³SO (49501), ³⁶SO (52502), S¹⁸O (50502), S¹⁷O (49502), SO⁺ (48010), ¹⁷OCS (61504), OC³⁶S (64510), ¹⁸OC³⁴S (64511), ¹⁸O¹³CS (63503), O¹³C³⁴S (63502), O¹³C³³S (62507), CS $v = 0 - 4$ (44501), CS⁺ (44512), ¹³C³⁶S (49508), H₂C³⁴S (48508), H₂C³³S (47506), H₂³³CS (47505), H₂S (34502), D₂S (36503), D₂³⁴S (38507), cis-HOSO⁺ (65510), Si³⁴S $v = 0 - 2$ (62508), Si³³S (61508), Si³⁶S (64514), ²⁹SiS $v = 0 - 2$ (61506), ³⁰SiS $v = 0 - 2$ (62510), ²⁹Si³⁴S $v = 0, 1$ (63504), ²⁹Si³³S (62512), ²⁹Si³⁶S (65507), ³⁰Si³⁴S $v = 0, 1$ (64513), ³⁰Si³³S (63505), ³⁰Si³⁶S (66505), SiS $v = 0 - 5$ (60506), HSiS (61512), H₂SiS (62513), OSiS (76517), HOCS⁺ (61510), HSCO⁺ (61509), t-HC(O)SH (62515), c-HC(O)SH (62516), SH⁺ (33505), HSO (49512), NS $v = 1$ (46516), N³⁴S (48509), N³³S (47509), N³⁶S (50516), ¹⁵NS (47510), DNCS a-type (60510), DNCS b-type (60511), HN¹³CS a-type (60512), H¹⁵NCS a-type (60513), HNC³⁴S a-type (61519), C₃S $v = 0$ (68503), C₃S $v_5 = 1$ (68505), C¹³CCS (69502), ¹³CCCS (69503), CC¹³CS (69507), C³⁴₃S (70502), CC¹³C³⁴S (71503), C¹³CC³⁴S (71504), ¹³CCC³⁴S (71505), C¹³C¹³CS (70506), ¹³CC¹³CS (70507), OC₃S (84502), H₂C₃S (70503), C₄S (80501), C₅S (92501), ¹³CC₄S (93501), C¹³CC₃S (93502), C₂¹³CC₂S (93503), C₃¹³CCS (93504), C₄¹³CS (93505), C³⁴₃S (94502), CaS $v = 0, 1$ (72501), ScS (77509), ⁴⁶TiS (78503), TiS (80505), ⁵⁰TiS (82503), YS (121502).

The following species have not been detected, because they do not have lines in the frequency range surveyed with PILS Band 7 data: CS $v = 1 - 0, 2 - 1$ (44510), CS $v = 2 - 0$ (44511), C³⁴S $v = 1 - 0$ (46510); ¹³CS $v = 0, 1$ (45501); ¹³CS $v = 1 - 0$ (45509); ¹³C³⁴S (47501), ¹³C³³S (47501), H₂³⁴S (36504), H₂³³S (35503), Si³⁴S $v = 1 - 0$ (62509), ²⁹SiS $v = 1 - 0$ (61507), ³⁰SiS $v = 1 - 0$ (62511), SiS $v = 1 - 0, 2 - 1$ (60507), SiS $v = 2 - 0$ (60508), S (32511), SH⁻ (33504), NS $v = 1 - 0$ (46517), ¹⁵N³⁴S (49511), HS $v = 0$ (33508), HS $v = 1$ (33509), H¹³CS⁺ (46504), HSCH₂CN (73503), HCNS (59510), HSNC (59511), HS¹³CN (60514), DSCN (60515), HSC¹⁵N (60516), H³⁴SCN (61520), C₇S (116501).

Finally, the following is a list of all other non-detected species at the 1σ level ($\sigma = 10$ mJy beam⁻¹ channel⁻¹ or 5 mJy beam⁻¹ km s⁻¹) that are available only in the JPL catalogue and their corresponding JPL entries in brackets: MgS (56009), ¹³CCS (57001), C¹³CS (57002), CC³⁴S (58001), PS (63007), SO₂ $v = 2$ (64005), H₂SO₄ (98001), SD (34005) does not have lines in the frequency range surveyed with PILS Band 7 data.

APPENDIX E: COMPARISON WITH A MODEL OF HOT CORES

Efforts on chemical modelling of sulphur networks have recently been revived by Woods et al. (2015). The authors computed the abundances of sulphur-bearing species for hot core conditions upon the inclusion of recent experimental and theoretical data into their chemical network, including a refractory sulphur residue. The modelled molecular ratios (relative to either H₂S or OCS; as tabulated

in table 9 of Woods et al. (2015) for the standard model with the interstellar cosmic ray ionization rate of 1.3×10^{-17} s⁻¹) can be compared to those derived in this work for IRAS 16293–2422 B. The exact values are given in Table E1. An agreement within one order of magnitude is found for OCS and CS relative to H₂S, and for H₂S relative to OCS. The modelled ratios for H₂CS are three orders of magnitude higher, which may be explained by the fact that the grain-surface network used in the models is fairly small and the grain-surface chemistry is not accounted for in full. H₂CS is expected to be involved in many grain-surface reactions and will likely be used up for synthesis of larger sulphur-bearing species, such as CH₃SH (analogous to the sequential hydrogenation of CO leading to CH₃OH with H₂CO as an intermediate).

For SO and SO₂, the differences are many orders of magnitude between the observed and modelled values of Woods et al. (2015). This likely has to do with the fact that the models have been run for a very long time of 10⁷ yr, which implies that many gaseous species are driven into SO and SO₂, leading to their overproduction. At earlier times (as seen in fig. 6 of Woods et al. 2015), the model results have a closer agreement for SO with observations. SO₂ remains too high nevertheless, which may have to do with thermal desorption being calculated via an efficiency factor. It seems that the modelling approach of Woods et al. (2015) is insufficient at reproducing the sulphur chemistry towards IRAS 16293–2422 B. The differences with cometary ROSINA measurements are just as large. The development of a full gas-grain chemical network for sulphur, including grain-surface chemistry, is the topic of future research. For the case of dark prestellar core, Vidal et al. (2017) have been able to successfully reproduce observed abundances of sulphur-bearing species without the need for artificial sulphur depletion.

A comparison with observations of hot cores, such as Sgr B2(N), Sgr B2(M) (e.g., Belloche et al. 2013) and Orion KL (e.g., Esplagues et al. 2014) is beyond the scope of this paper due to the mandatory discussion on emitting regions and structures sampled with observations. Future high spatial resolution ALMA observations will mediate this problem.

This paper has been typeset from a $\text{\TeX}/\text{\LaTeX}$ file prepared by the author.

Table E1. Molecular ratios relative to H₂S and OCS as measured with these interferometric ALMA observations at the one beam offset position from source B of IRAS 16293–2422^a in comparison to hot core models^f

| Species | Molecular ratios relative to H ₂ S (%) | | Molecular ratios relative to OCS (%) | |
|-------------------|---|-------------------|--------------------------------------|-------------------|
| | ALMA B | model | ALMA B | model |
| H ₂ S | 100 | 100 | 68 – 679 | 29 |
| OCS | 147 – 15 | 341 | 100 | 100 |
| SO | 0.3 – 0.03 | 58 | 0.2 | 17 |
| SO ₂ | 0.8 – 0.08 | 1.5×10^4 | 0.5 | 4.5×10^3 |
| CS | 2 – 0.2 | 1.2 | 2 | 0.3 |
| H ₂ CS | 0.8 | 129 | 0.5 | 38 |

^a values taken from Table 3

^f table 9 of Woods et al. (2015) for the standard model with the interstellar cosmic ray ionization rate of $1.3 \times 10^{-17} \text{ s}^{-1}$